Research Square

Preprints are preliminary reports that have not undergone peer review.
They should not be considered conclusive, used to inform clinical practice,
or referenced by the media as validated information.

Integrative multi-omics analysis of the CALM3-FRMD6-AS2 regulatory axis in gastric cancer reveals single-cell heterogeneity and enables construction of a prognostic model

Fan Luo
Lanzhou University
Xuelian Shu
Lanzhou University
Luyao Cheng
Lanzhou University
Yilin Wang
Lanzhou University
Jing Li
Lanzhou University
Ren Man
renman1983@163.com

The First Hospital of Lanzhou University

Research Article

Keywords: gastric cancer, single-cell transcriptomics, cancer-associated fibroblasts, CALM3, FRMD6-AS2, RNA-binding protein, epithelial-mesenchymal transition, in silico gene perturbation, prognostic model, multi-omics integration

Posted Date: November 17th, 2026

DOI: https://doi.org/10.21203/rs.3.rs-11358791/v1

License: This work is licensed under a Creative Commons Attribution 4.0 International License.
Read Full License

Additional Declarations: No competing interests reported.

Integrative multi-omics analysis of the CALM3-FRMD6-AS2 regulatory axis in gastric cancer reveals single-cell heterogeneity and enables construction of a prognostic model

Abstract

Gastric cancer exhibits high tumour heterogeneity, which hinders precision treatment. Beyond canonical calcium-signalling roles, CALM3 acts as an RNA-binding-protein, while the lncRNA FRMD6-AS2 remains poorly characterised in gastric-cancer tumour microenvironment, especially in cancer-associated fibroblasts (CAFs). This study integrated TCGA-STAD bulk transcriptome and GSE183904 single-cell datasets to characterise the CALM3-FRMD6-AS2 regulatory axis. Multiple bioinformatic algorithms predicted their potential physical interaction. Single-cell analysis identified FRMD6-AS2 as an extremely rare CAF-specific lncRNA expressed in only 0.034 % of total cells. In silico perturbation demonstrated that FRMD6-AS2 knockdown disturbed the ZEB1-CDH1 epithelial axis and activated mesenchymal programmes, and CALM3 gradient rescue could not reverse epithelial damage, indicating their parallel-synergistic non-redundant regulation of EMT. qPCR, CCK-8, flow cytometry and scratch-wound-healing assays in HGC-27 cells validated that FRMD6-AS2 knockdown suppressed proliferation, promoted apoptosis and enhanced migration, whereas CALM3 over-expression exerted opposite cellular phenotypes. A LASSO-Cox-derived prognostic risk model incorporating CALM3-FRMD6-AS2 and clinical factors showed favourable predictive performance and consistent risk trends across external GEO cohorts. Bulk-omics negative results supported the signal-dilution effect caused by this rare CAF sub-population. In conclusion, the CALM3-FRMD6-AS2 axis marks a rare malignant CAF subset and cooperatively drives EMT-related malignant progression in gastric cancer, offering novel insights for CAF heterogeneity research and stroma-targeted therapeutic strategies.

Keywords: gastric cancer; single-cell transcriptomics; cancer-associated fibroblasts; CALM3; FRMD6-AS2; RNA-binding protein; epithelial-mesenchymal transition; in silico gene perturbation; prognostic model; multi-omics integration

1 Introduction

Gastric cancer is a globally prevalent malignant disease, ranking fifth in incidence and third in mortality worldwide. Despite advances in endoscopic screening, chemotherapy and immune-checkpoint-inhibitor-based immunotherapy, the 5-year overall survival rate for advanced gastric cancer remains below 30 %[1]. High molecular heterogeneity within tumors and the tumor microenvironment (TME) constitutes a major barrier to improved therapeutic outcomes. Conventional TNM staging relies solely on anatomical invasion status, disregarding functional heterogeneity among cellular subsets inside the TME[2-4]; therefore, it cannot precisely stratify patients according to long-term survival risk. There is an urgent demand for molecular prognostic biomarkers and novel regulatory mechanisms derived from microenvironmental characteristics.

Cancer-associated fibroblasts (CAFs) represent the most abundant stromal cell population within the gastric-cancer TME. By remodeling the extracellular matrix, secreting chemokines and modulating immune-cell infiltration, CAFs continuously facilitate tumor proliferation, invasion and metastasis[5-6]. Recent studies have confirmed profound functional heterogeneity within the CAF compartment. A small fraction of rare malignant CAF subsets exert potent pro-tumorigenic, pro-metastatic and stem-cell-like properties and serve as key drivers of malignant progression[7-8]. Nevertheless, the core molecular axes governing activation and functional remodeling of such rare malignant CAF subsets have not been systematically characterized.

CALM3 (Calmodulin-3) is classically known for mediating intracellular calcium-signal transduction[9]. Recent reports have uncovered its non-canonical RNA-binding-protein activity: it can bind lncRNAs to modulate transcript stability and downstream-pathway activation and participates in progression of gastrointestinal malignancies[10]. FRMD6-AS2 is an antisense lncRNA transcribed from the *FRMD6* locus. Prior work suggested its involvement in Hippo-pathway regulation[11-12]; however, its cell-type-specific expression, functional features and molecular regulatory mechanisms within the gastric-cancer TME, especially within rare CAF subsets, remain unreported.

Epithelial-mesenchymal transition (EMT) is a core biological program underlying gastric-cancer invasion and metastasis[13-14], driven by dynamic imbalance between the ZEB1-CDH1 epithelial axis and the *VIM*/*FN1* mesenchymal axis[15-17]. To date, no studies have addressed whether the CALM3-FRMD6-AS2 axis participates in EMT remodeling in gastric cancer; furthermore, their upstream-downstream relationship and functional complementarity remain unclear. Single-cell in silico gene knockout and rescue perturbation represent powerful computational experimental tools for dissecting molecular-regulatory logic within rare cellular subsets.

In the present study, we integrated TCGA bulk transcriptomic data and the GSE183904 single-cell dataset. Candidate CALM3-FRMD6-AS2 interactions were screened by combining WGCNA and multiple prediction algorithms. We deciphered transcriptional and microenvironmental features of the FRMD6-AS2^{+} rare malignant CAF subpopulation. Single-cell gradient in silico knockout and CALM3 rescue simulations were implemented to elucidate for the first time the parallel-synergistic mechanism governing EMT regulation. A highly robust prognostic model was constructed and externally validated across multiple cohorts. We systematically interpreted the signal-dilution mechanism that reconciles pathway activation observed in single-cell data with negative results in bulk-omics cohorts. Our findings deliver novel candidate targets and theoretical foundations for precise patient stratification and stroma-directed therapy for gastric cancer.

2 Materials and Methods

2.1 Acquisition and differential-expression analysis of TCGA data

STAR-Counts RNA-seq count matrices for TCGA-STAD were downloaded from the GDC database via TCGAbiolinks (v2.30.0), encompassing 448 samples (412 tumor samples and 36 adjacent non-tumor controls)[18]. GENCODE v36 annotation files were used to discriminate mRNAs from lncRNAs, and the rtracklayer package was utilized to extract the lncRNA expression matrix[19]. Differential-expression analysis was performed with DESeq2 (v1.44.0). Screening thresholds were set as $|\log_2 FC| > 1$ and $P < 0.05$.

2.2 WGCNA weighted gene co-expression-network analysis

The WGCNA package (v1.72) was employed to build weighted gene co-expression networks using input sets consisting of differentially-expressed RBPs and lncRNAs[20]. The soft-threshold power was set to 17 (scale-free network $R^2 = 0.878$). Gene modules were partitioned by dynamic tree-cutting, with a minimum module size of 30 and a module-merging threshold of 0.2. Hub genes were screened according to within-module connectivity (*k*Within). A co-expression network diagram for the core module was plotted to visualize gene-gene interactions.

2.3 RNA secondary-structure prediction and RBP-lncRNA-binding prediction

ViennaRNA RNAfold (v2.6.3) predicted the secondary-structure and thermodynamic parameters of FRMD6-AS2 (581 nt). Three independent tools were used for cross-validation of CALM3-FRMD6-AS2 binding potential: ① catRAPID-omics v2.1 for interaction-propensity calculation; ② RPISeq v1.0 with random-forest and support-vector-machine models for binding-probability prediction; ③ RBPSuite2.0 for segment-wise binding-score calculation. Interaction confidence was comprehensively judged based on outputs from all three tools.

2.4 Single-cell-transcriptome data processing, cell-subset annotation and signature construction

The single-cell dataset GSE183904 was retrieved from the GEO database[21], containing 31 primary gastric-cancer lesions and 40 sequencing libraries totalling 158 641 single cells generated on the 10x Genomics NovaSeq 6000 platform. Quality control and preprocessing were performed in Python (v3.11) using Scanpy (v1.9.8). Filtering criteria: *nFeature_RNA* > 200, *percent.mt* < 20 %. Finally, 158 641 high-quality cells and 26 571 expressed genes were retained. Log1p normalization was conducted, followed by PCA dimensionality reduction, UMAP clustering and cellular-identity annotation. Classic marker genes guided lineage annotation: *EPCAM*/*KRT8* for tumor epithelial cells; *VIM*/*COL1A1* for CAFs; *CD3D* for T-cells; *CD68* for macrophages; *MS4A1* for B-cells.

The Wilcoxon test was used to compare transcriptomes between FRMD6-AS2$^+$ CAFs and ordinary CAFs within Cluster 12. Screening criteria: *p_adj* < 0.05, $\log_2 FC > 0.5$. The top-50 significantly up-regulated genes were selected to build a signature specific for FRMD6-AS2$^+$ CAFs; discriminative performance was validated by internal single-cell-signature scoring. Cells with gene expression count > 0 were defined as FRMD6-AS2-positive cells. Note that 10X

Genomics single-cell data suffer from dropout events; therefore, this definition may underestimate the true number of FRMD6-AS2-expressing cells.

2.5 ssGSEA signature projection onto bulk cohorts and MCP-counter deconvolution

Genes from the 50-gene signature were intersected with genes present in the TCGA expression matrix. The GSVA package implemented ssGSEA to compute enrichment scores for the FRMD6-AS2^{+} malignant-CAF signature for each patient sample. MCP-counter estimated global fibroblast abundance based on pan-CAF marker genes. Spearman correlation analysis and Wilcoxon rank-sum tests were applied to assess associations between signature scores, CAF abundance and risk scores.

2.6 Enrichment analysis and cell-communication analysis

GO and KEGG enrichment analyses were performed with clusterProfiler (v4.12). GSVA calculated Hallmark-pathway activity scores. The CellChat package constructed ligand-receptor-mediated intercellular-communication networks and quantitatively measured intra-CAF self-communication strength as well as bidirectional communication strength between FRMD6-AS2^{+} CAFs and immune cells.

2.7 Single-cell in silico gene knockout, gradient perturbation and CALM3 rescue simulation

An expression matrix derived exclusively from the 52 FRMD6-AS2-positive cells was used to fit a linear-regression model for FRMD6-AS2 versus CALM3 and core EMT-related genes:$CALM3 = \beta_0 + \beta_1 \times FRMD6 - AS2 + \varepsilon,$ Model fitting was completed viasklearn.linear_model.LinearRegression.

Gradient-knockdown settings: FRMD6-AS2 expression was sequentially reduced to 70 %, 50 %, 30 %, 10 % and 1 % of baseline levels to predict dose-dependent changes in CALM3 expression.

Rescue-simulation settings: on the basis of 90 % FRMD6-AS2 knockout, CALM3 was virtually over-expressed at 2-fold, 5-fold and 10-fold levels. The percentage recovery of CALM3 expression was calculated, together with magnitude of expression reversal for core EMT genes (*VIM*, *CDH2*, *FN1*, *SNAI1*, *TWIST1*, *ZEB1*, *CDH1*).

2.8 Prognostic-model construction, inter-model comparison, external validation and multi-omics-association analysis

Six variables including CALM3, FRMD6-AS2, age group, gender, T-stage and N-stage were incorporated. LASSO-Cox regression was executed using the glmnet package; 10-fold cross-validation selected the optimal λ value to generate the risk-score formula. Four distinct models were built for horizontal comparison to quantify incremental prognostic value contributed by molecular markers: ① Base clinical-only model

(age + gender + T-stage + N-stage); ② CALM3-only model; ③ FRMD6-AS2-only model; ④ Integrated model (base-clinical variables + CALM3 + FRMD6-AS2).

Comparison metrics comprised C-index, time-dependent 1-, 3- and 5-year AUC values, and DCA decision-curve analysis. Patients were stratified into high-risk and low-risk subgroups using the median risk-score as the cut-off. Kaplan-Meier survival curves were plotted using the survival package; multivariate Cox regression identified independent prognostic factors. The timeROC package computed time-dependent AUC values. External-validation cohorts included GSE62254, GSE26253 and GSE15459. Z-score standardization was performed uniformly prior to risk-stratification and performance validation.

Immune-infiltration, TMB and pathway-activity analyses were implemented with ESTIMATE, xCell, maftools and GSVA. Multiple-testing correction adopted the Benjamini-Hochberg FDR procedure; FDR < 0.05 was defined as statistically significant.

2.9 Cell culture and transfection

The human gastric-cancer cell line HGC-27 was purchased from the Cell Bank of the Chinese Academy of Sciences. Cells were cultured in RPMI 1640 medium (Skejie Biotech, CF0002-500 mL) supplemented with 10 % fetal bovine serum (Invigentech, A6913), 100 U/mL penicillin and 100 μg/mL streptomycin, and incubated at 37 °C under 5 % CO_2 in a humidified incubator (LABGIC, COL-80P). Cells in logarithmic-growth phase were harvested for downstream experiments.

Four experimental groups were set: siNC, siLincRNA (si-FRMD6-AS2), oeNC and oeCALM3. siRNA and over-expression plasmids were transfected using Lipofectamine 3000 (Invitrogen) following manufacturer protocols. Cells were harvested 48 h post-transfection for subsequent assays.

2.10 RNA extraction, cDNA synthesis and qPCR assay

Total RNA was extracted using TransZol Up reagent. Briefly, 0.2 mL RNA-Extraction Agent was added; samples were vortexed and incubated at room temperature for 5 min. After centrifugation (12 000 rpm, 4 °C, 15 min), the colourless aqueous upper phase was transferred to fresh tubes without aspirating the white interphase layer. An equal volume of isopropanol was added for RNA precipitation (10 min at room temperature). RNA pellets were collected by centrifugation (12 000 rpm, 4 °C, 10 min), washed once with 1 mL 75 % ethanol (7 500 rpm, 5 min), air-dried in a fume hood for ~10 min, resuspended in RNase-free water and stored at −80 °C after aliquoting.

RNA concentration and purity were quantified with a micro-volume spectrophotometer; acceptable A260/A280 ratios ranged from 1.8 to 2.1.

cDNA synthesis was performed on-ice in a total reaction volume of 20 μL: 10 μL total RNA, 2 μL 8 × gDNA remover, 4 μL RNase-free dH_2O; incubation at 42 °C for 2 min. Then 4 μL

5 × RT SuperMix was added. Thermal-cycler conditions: 55 °C for 15 min, 85 °C for 5 sec. Synthesized cDNA was chilled on-ice immediately and stored at −20 °C.

Real-time qPCR was carried out in a total 20-μL reaction system containing 10 μL 2 × SYBR Premix Ex Taq Ⅱ (Tli RNaseH Plus), 2 μL cDNA template (50 ng), 0.4 μL forward primer (10 μM), 0.4 μL reverse primer (10 μM), 7.2 μL RNase-free dH_2O. Each sample was assayed in technical triplicate. Thermal-cycling protocol: Step 1: 95 °C for 120 s (1 cycle); Step 2: 40 cycles of 95 °C for 30 s, 60 °C for 60 s; melting-curve acquisition: 95 °C for 10 s, 60 °C for 60 s, 95 °C for 10 s. Amplification and melting curves were inspected to validate data quality. Primer sequences: *GAPDH*: forward 5′-GTGGACCTGACCTGCCGTCTAG-3′; reverse 5′-GAGTGGGTGTCGCTGTTGAAGTC-3′, amplicon length 149 bp. *FRMD6-AS2*: forward 5′-ATGGGTACACTCAGAGGCCA-3′; reverse 5′-CAGAGGCATTTGGTTGAGCC-3′, amplicon length 88 bp. *CALM3*: forward 5′-AGGGTGGGGACGAGAGATTC-3′; reverse 5′-TGCTTCAGTGGGGTTCTGTC-3′, amplicon length 170 bp.

2.11 CCK-8 cell-proliferation assay

Cells were seeded into 96-well plates at a density of 1 × 10^4 cells per well; six technical replicates were prepared for each group. At 24 h, 48 h and 72 h time-points, 10 μL CCK-8 reagent (Solarbio, CA1210) was added per well and plates were incubated for 2 h. Absorbance (OD_{450}) was read using a Thermo Mk3 microplate reader. OD values were recorded; cell viability relative to control groups was calculated. GraphPad Prism software was used for plotting. One-way ANOVA followed by Tukey's multiple-comparison test was used for inter-group statistical comparisons; $P < 0.05$ was considered statistically significant.

2.12 Flow-cytometry apoptosis detection

The Annexin V-FITC/PI Apoptosis Kit (Lianke Biotech, AT101C) was used. HGC-27 cells were seeded into 6-well plates at 3 × 10^5 cells/well and cultured for 24 h post-transfection. Cells were harvested and adjusted to 1 × 10^6 cells/mL in 1 × Binding-Buffer. Unstained control tubes, single-stain compensation tubes and sample tubes were prepared. Sample tubes received 5 μL Annexin V-FITC and 10 μL PI. After gentle mixing, samples were incubated in the dark at room temperature for 30 min and analysed on a flow cytometer. SPSS Statistics 21 performed statistical analysis; one-way ANOVA with Tukey's post-hoc test was applied for pairwise comparisons. GraphPad Prism generated graphs; $P < 0.05$ represented statistical significance.

2.13 Scratch-wound-healing migration assay

Transfected HGC-27 cells were seeded into 6-well plates at 3 × 10^5 cells/well and cultured overnight. A sterile pipette tip held perpendicular to the plate surface created uniform scratches. Floating cells were washed away three times with PBS, and medium containing 1 % FBS was added. Baseline images (0 h) were captured; plates were incubated for another 24 h before second-time imaging. Image-Pro-Plus software quantified wound-closure distances.

Repeated-measures ANOVA was used for statistical comparisons. GraphPad Prism was used for plotting; $P < 0.05$ was considered statistically significant.

2.14 Statistical analysis

Bulk-omics statistics were implemented in R 4.4.2; single-cell in-silico-perturbation statistics were performed in Python 3.11 with SciPy (v1.11.4). Two-group continuous-variable comparisons used Wilcoxon rank-sum tests; correlation analyses applied Pearson or Spearman correlation coefficients. Survival analyses used Log-rank tests and Cox regression models. The Benjamini-Hochberg correction controlled for multiple-testing bias; FDR < 0.05 was defined as statistically significant.

Wet-laboratory functional-experiment data are presented as mean ± SD and analysed using SPSS Statistics 21 and GraphPad Prism. Two-group comparisons used independent-sample *t*-tests. Multiple-group comparisons adopted one-way ANOVA with Tukey's post-hoc test. Repeated-measures ANOVA was used for time-series data. $P < 0.05$ was regarded as statistically significant.

---

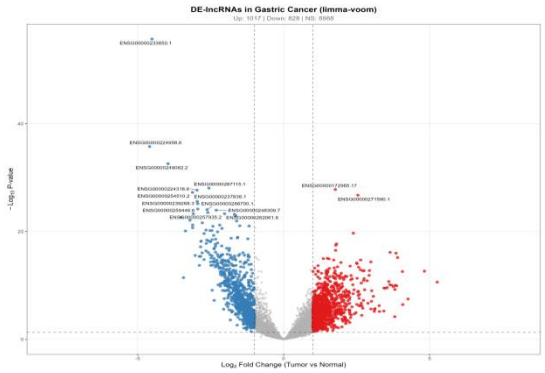
3 Results

3.1 Differential-expression analysis of TCGA-STAD and WGCNA co-expression-network analysis

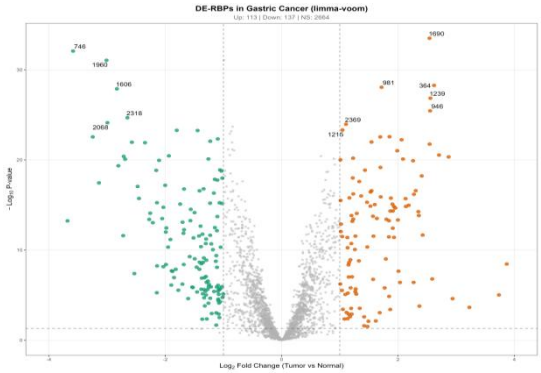
To systematically identify aberrantly expressed lncRNAs and RBPs in gastric cancer, differential-expression analysis was performed on the TCGA-STAD dataset. Among 15 410 expressed lncRNAs, 1 845 were differentially-expressed ($|\log_2 FC| > 1$, $P < 0.05$), of which 1 017 (55.1 %) were up-regulated in tumours and 828 (44.9 %) down-regulated. Among 2 999 RBPs, 250 exhibited differential expression: 113 (45.2 %) up-regulated and 137 (54.8 %) down-regulated (Figure 1A-B). The number of differentially-expressed lncRNAs greatly exceeded that of differentially-expressed RBPs (1 845 vs. 250), implying broader and more active roles for lncRNAs in gastric-carcinogenesis.

Four gene modules were identified via WGCNA. The MEblue module was positively and significantly correlated with T-stage ($r = 0.164$, $P = 0.002$) and poor prognosis ($r = 0.131$, $P = 0.010$), and was designated the core oncogenic module containing 573 genes (521 lncRNAs, 52 RBPs). CALM3 was the hub RBP with the highest intra-module connectivity (*k*Within = 7), predicted to regulate seven lncRNA transcripts. Among these, FRMD6-AS2, an antisense lncRNA transcribed from the *FRMD6* locus (a known Hippo-pathway regulator), was selected as the top candidate interaction partner for CALM3 for downstream analyses. The MEblue-module co-expression network visually illustrated the co-expression linkage between CALM3 and FRMD6-AS2 (Figure 1C-G).

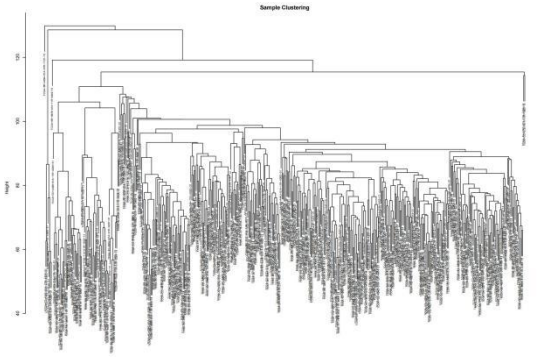
A


DE-lncRNAs in Gastric Cancer (limma-voom)
Up: 1017 | Down: 629 | NS: 8998
-Log10 Pvalue
Log2 Fold Change (Tumor vs Normal)

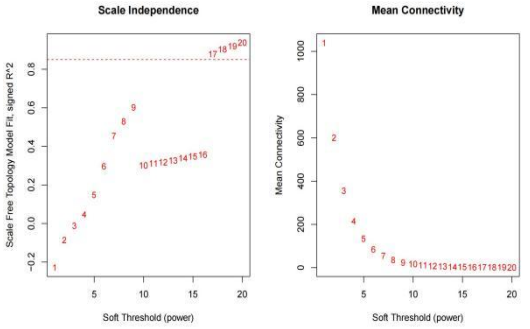
B


DE-RBPs in Gastric Cancer (limma-voom)
Up: 113 | Down: 137 | NS: 2664
-Log10 Pvalue
Log2 Fold Change (Tumor vs Normal)

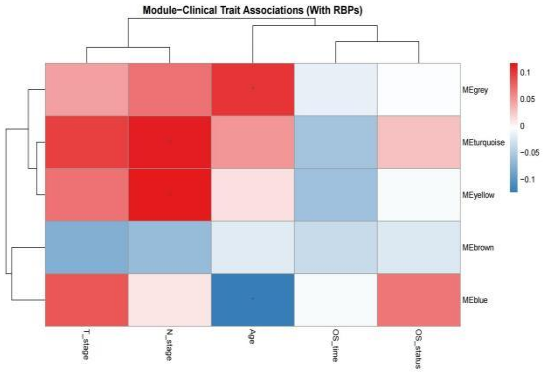
C


Sample Clustering
Height

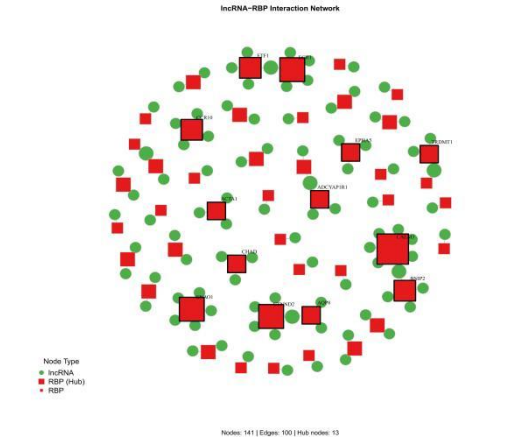
D


Scale Independence
Scale Free Topology Model Fit, signed R^2
Soft Threshold (power)
Mean Connectivity
Mean Connectivity
Soft Threshold (power)

E


Module−Clinical Trait Associations (With RBPs)
MEgrey
MEturquoise
MEyellow
MEbrown
MEblue
T_stage
N_stage
Age
OS_time
OS_status

F


lncRNA−RBP Interaction Network
Node Type
lncRNA
RBP (Hub)
RBP
Nodes: 141 | Edges: 100 | Hub nodes: 13

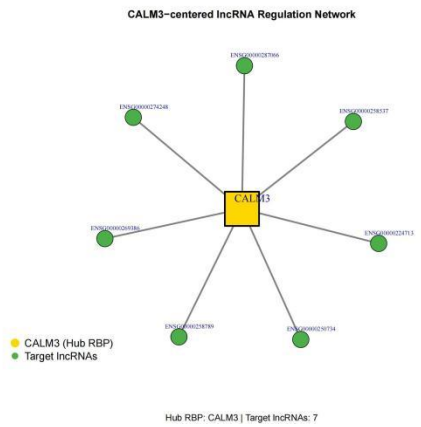
G	H
	

Figure 1 (A-B) Volcano plots showing differentially-expressed lncRNAs and RBPs in TCGA-STAD gastric-cancer cohort. (C) Sample-clustering dendrogram for WGCNA. (D) Soft-threshold-power selection for scale-free-network construction (scale-independence and mean-connectivity curves). (E) Heat-map depicting module-versus-clinical-trait associations. (F) Global lncRNA-RBP interaction-network diagram. (G) CALM3-centred lncRNA-regulatory sub-network.

3.2 Secondary-structure prediction of FRMD6-AS2 and CALM3-binding-potential prediction

FRMD6-AS2 totals 581 nt in length with a GC content of 40.10 %. RNAfold predicted a minimum-free-energy (MFE) of −150.30 kcal/mol, supporting stable stem-loop secondary-structure formation; ensemble diversity = 102.67 indicates relatively high conformational heterogeneity, which favours non-canonical RBP binding to single-stranded RNA segments (Figure 2A-B).

Consistent outputs from three independent prediction tools supported potential interaction: catRAPID interaction propensity = 11.07 (> 10 indicates strong binding), Z-score = −0.15, CALM3 RNA-binding propensity = 0.68; RPISeq random-forest probability = 0.612, SVM probability = 0.567 (Figure 2C); RBPSuite-2.0 segment-wise scores for segments 3, 5, 8 reached 0.89, 0.79 and 0.91 respectively, all above the 0.5 threshold (Figure 2D). Collectively, the results predict high-confidence potential physical interaction between CALM3 and FRMD6-AS2.

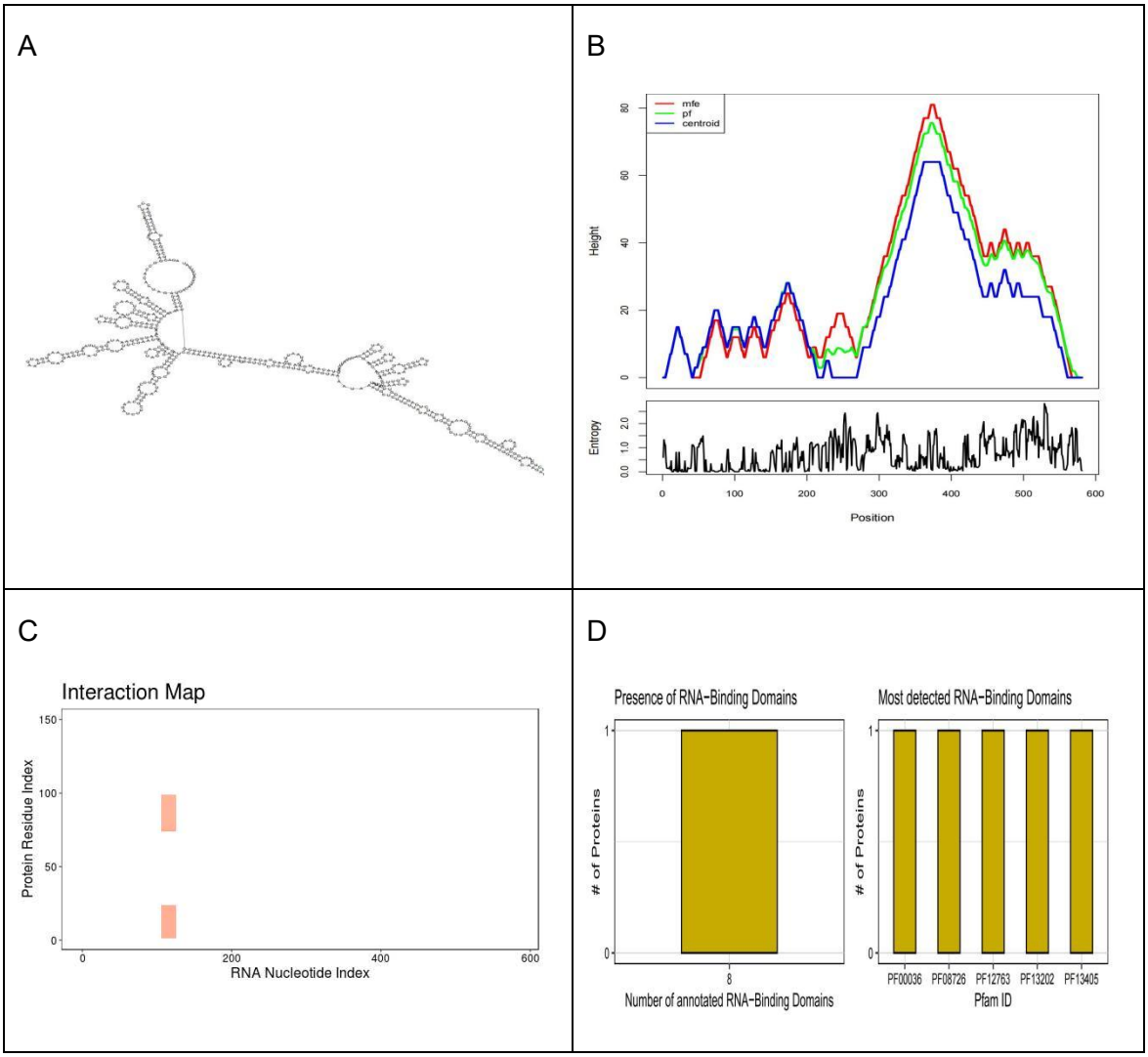


Figure 2 (A-B) Predicted RNA secondary-structure of FRMD6-AS2. (C) catRAPID interaction-residue-map. (D) RBPSuite-2.0 RNA-binding-domain annotation summary.

3.3 Construction of the gastric-cancer single-cell transcriptomic atlas

After quality-control filtering, 158 641 high-quality single-cell profiles were retained. UMAP dimensionality-reduction and clustering resolved 25 cellular clusters, including tumour epithelial cells (Tumor_Epi, 85.3 %), T-lymphocytes (T_cell, 4.2 %), macrophages (Macrophage, 4.0 %), B-lymphocytes (B_cell, 3.3 %) and cancer-associated fibroblasts (CAF_Cluster12, 3.2 %) (Figure 3A-E).

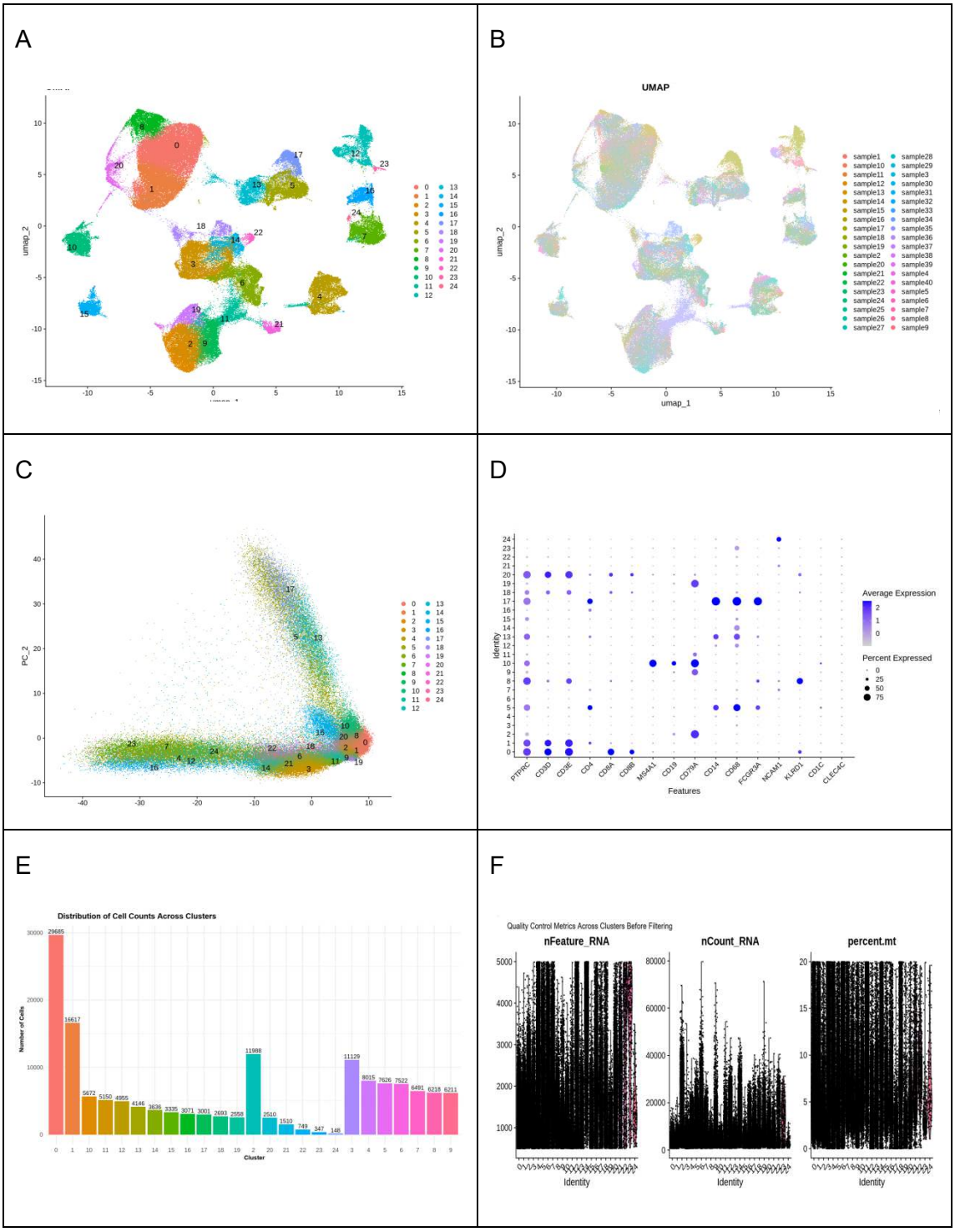


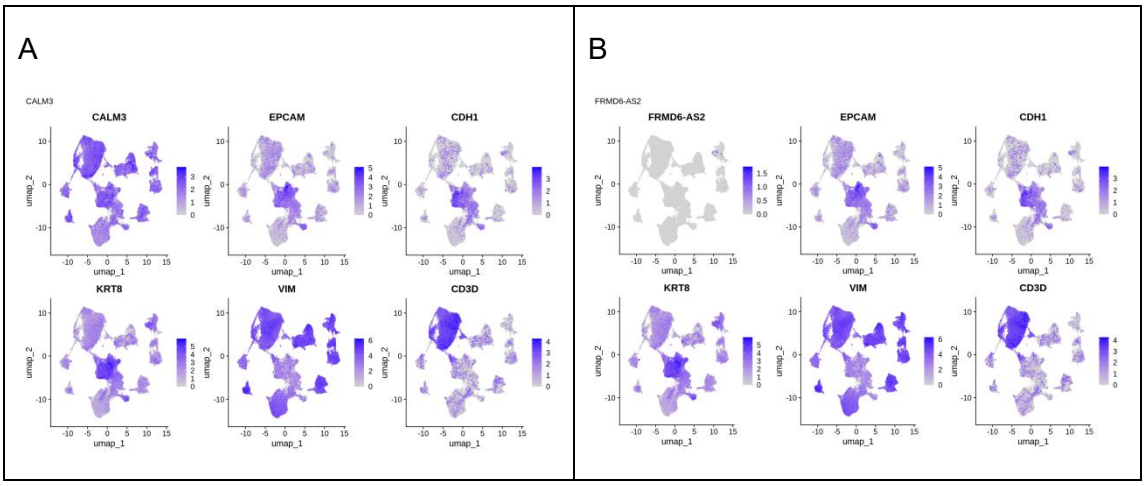
Figure 3 (A) UMAP plot coloured by cell-cluster identity. (B) UMAP plot coloured by sample origin. (C) PCA dimensionality-reduction plot. (D) Dot-plot showing canonical cell-lineage-marker-gene expression. (E) Bar-chart showing cell-count distribution across clusters. (F) Violin-plots for QC metrics (*nFeature_RNA*, *nCount_RNA*, *percent.mt*) per cluster.

3.4 Single-cell-expression patterns of CALM3 and FRMD6-AS2

CALM3 was detected in 61 134 cells (39.45 % of total cells), with mean expression = 0.5216 and maximum expression = 3.7664. CALM3 expression exhibited substantial heterogeneity across cell clusters. Highest CALM3-positive fractions occurred among tumour-epithelial-cell clusters: Cluster 21 (80.08 %), Cluster 15 (75.94 %), Cluster 23 (75.30 %), Cluster 24 (72.05 %), Cluster 18 (66.94 %), Cluster 17 (63.17 %), Cluster 13 (61.84 %). In contrast, T-cell (Cluster 7), macrophage (Cluster 9) and B-cell (Cluster 11) clusters showed markedly reduced CALM3-positive proportions (all < 30 %), indicating predominant CALM3 expression within tumour epithelial compartments (Figure 4A).

FRMD6-AS2 exhibited extremely rare expression, detected in only 52 cells (0.034 % of all cells), with mean expression = 0.5512 and maximum expression = 1.7403. Its distribution was highly restricted: 49 positive cells (94.2 %) mapped to the CAF-containing Cluster 12 and merely three cells (5.8 %) mapped to T-cell Cluster 7, identifying FRMD6-AS2 as a CAF-enriched lncRNA (Figure 4B).

Co-expression analysis within FRMD6-AS2-positive cells showed that 39 cells (75 %) were CALM3-FRMD6-AS2 double-positive, whereas 13 cells (25 %) were FRMD6-AS2-single-positive (CALM3-negative). These observations suggest that FRMD6-AS2 activation is not entirely dependent on high CALM3 abundance, although this interpretation is confounded by single-cell-sequencing dropout events (Figure 4C).



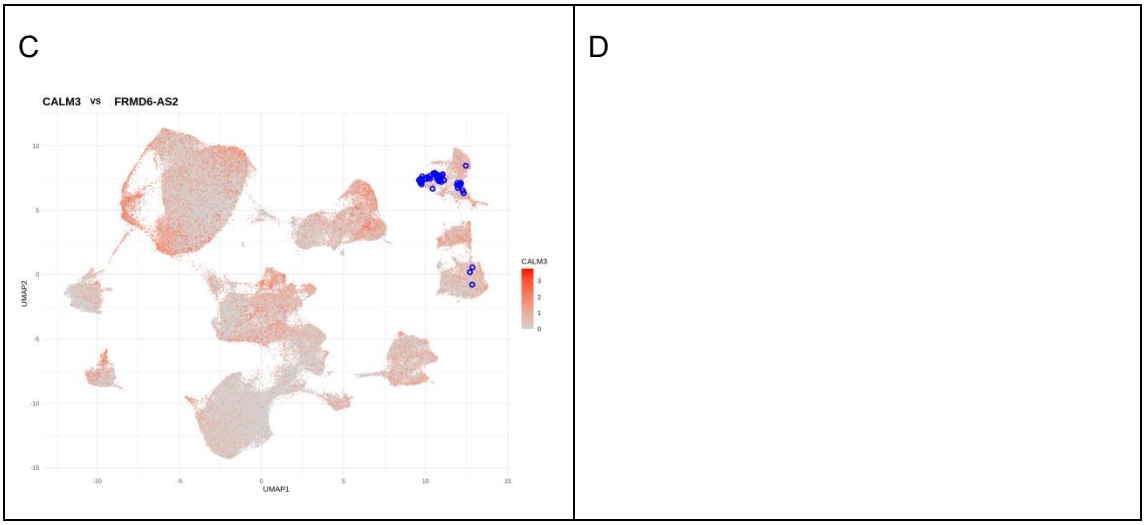


Figure 4 (A) Feature-plots for CALM3 and canonical cell-lineage markers. (B) Feature-plots for FRMD6-AS2 and canonical cell-lineage markers. (C) UMAP dual-variable spatial mapping plot

3.5 Transcriptional features of FRMD6-AS2^{+} CAFs and construction of its specific signature

Comparing transcriptomes of FRMD6-AS2^{+} CAFs versus ordinary CAFs within Cluster 12 yielded 6 631 differentially-expressed genes; 572 genes were significantly up-regulated (*p_adj* < 0.05, $\log_2$FC > 0.5), among which FRMD6-AS2 represented the most strongly up-regulated gene ($\log_2$FC = 11.99) (Figure 5A).

Top up-regulated signature genes included *ALDH8A1* ($\log_2$FC = 3.49), *PACRG* ($\log_2$FC = 3.57), *FGD3* ($\log_2$FC = 3.56), *SERPINE3* ($\log_2$FC = 3.38), *ANO5* ($\log_2$FC = 3.27), *GPR85* ($\log_2$FC = 3.56). Functionally, high *ALDH8A1* indicates dysregulated retinoic-acid metabolism; *PACRG* and *FGD3* govern cytoskeleton remodelling and invasive phenotypes; *SERPINE3* participates in ECM degradation and stromal remodelling; *ANO5* mediates calcium-ion signalling, functionally cross-linking with CALM3-dependent calcium-regulatory pathways(Figure 5B).

The top-50 up-regulated genes were assembled into the FRMD6-AS2^{+}-CAF-specific signature. Signature enrichment scores were significantly higher within FRMD6-AS2^{+} CAFs relative to ordinary CAFs and all other cellular subsets (P < 0.001), verifying that this gene-set can specifically discriminate this malignant CAF subtype(Figure 5C-D).

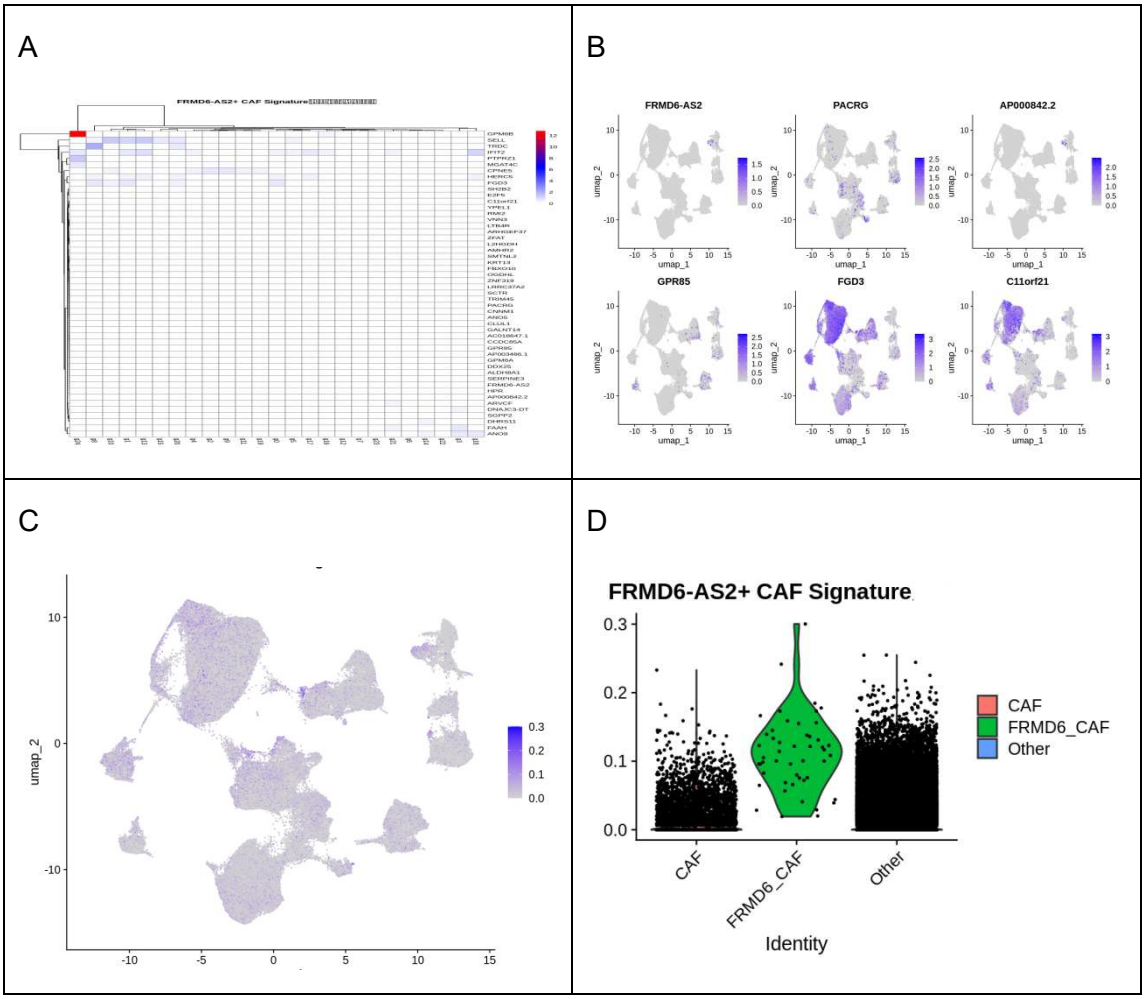


Figure 5 (A) Heat-map of the 50-gene FRMD6-AS2⁺-CAF signature across single-cell clusters. (B) Feature-plots of representative signature-gene expression. (C) UMAP visualisation of FRMD6-AS2⁺-CAF-signature scores. (D) Violin-plot comparing signature-score distributions among ordinary CAFs, FRMD6-AS2⁺ CAFs and other-cell populations.

3.6 GSEA enrichment and CellChat cell-communication analysis

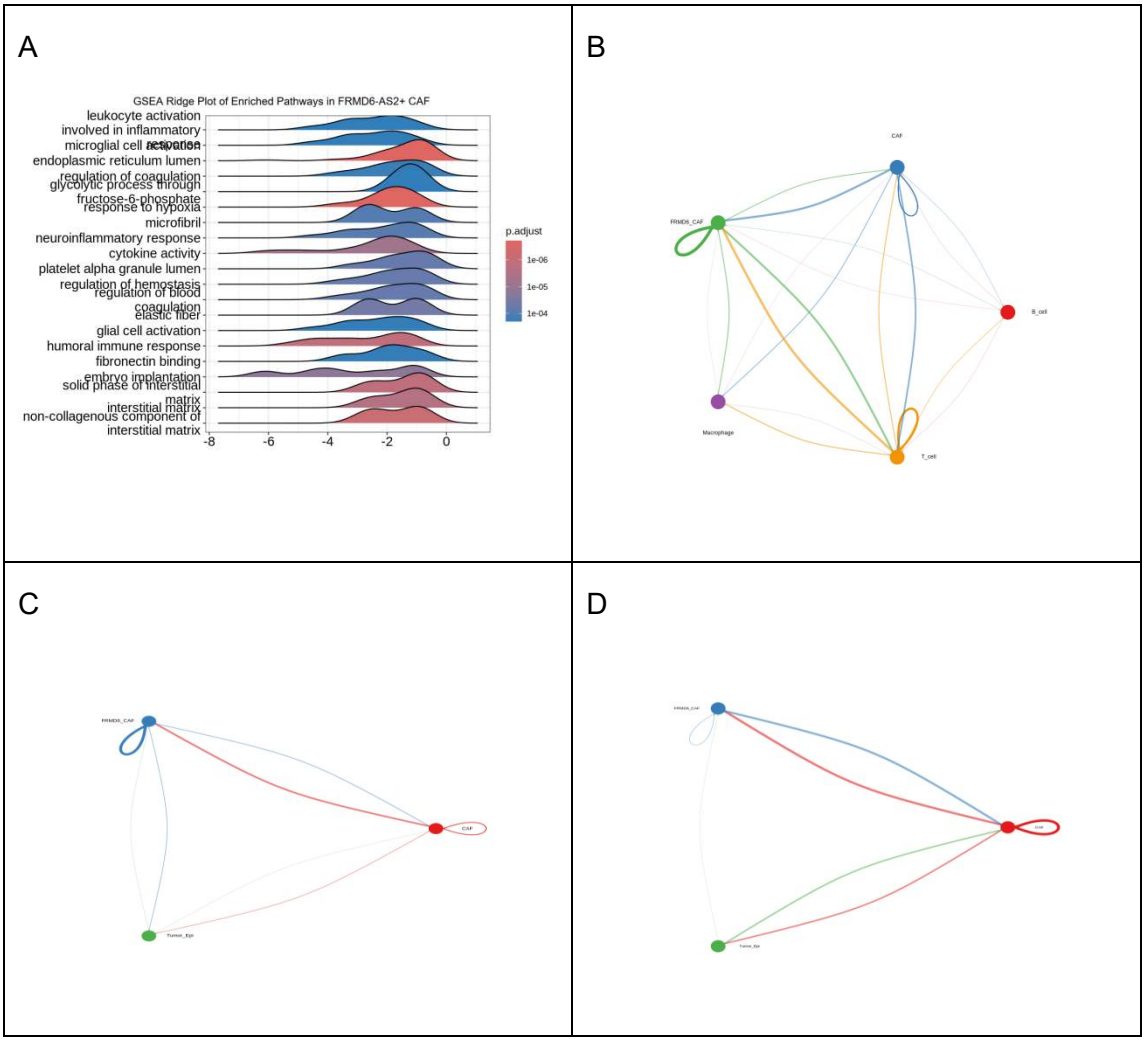
GSEA revealed significant enrichment of ALDH-related activity (NES = 2.13, P < 0.001), redox-process, diterpenoid-metabolism and retinoic-acid-metabolism gene-sets in FRMD6-AS2⁺ CAFs, further supporting stem-cell-like metabolic phenotypes for this subset(Figure 6A).

CellChat deconvoluted intercellular-communication networks. When only tumour-epithelial-cell and CAF populations were included, 30 signalling pathways were detected, dominated by ECM-associated signals (*COLLAGEN*, *LAMININ*) and growth-factor pathways (*VEGF*, *PDGF*, *FGF*). Strong intra-subset self-communication existed among FRMD6-AS2⁺ CAFs. After incorporating all immune-cell populations, 38 signalling pathways were identified, additionally

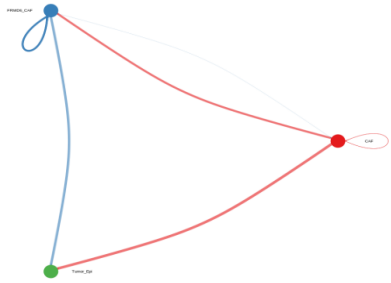
including CXCL-chemokine, *PERIOSTIN* and *VISFATIN* axes. Bidirectional communication strengths: FRMD6-AS2$^+$ CAFs → T-cells = 72; T-cells → FRMD6-AS2$^+$ CAFs = 87. Communication strength: FRMD6-AS2$^+$ CAFs → macrophages = 32; FRMD6-AS2$^+$ CAFs → B-cells = 7. FRMD6-AS2$^+$ CAFs highly expressed *CXCL1*, *CXCL8* and *CXCL14*, with cognate receptors *CXCR1*/*CXCR2*/*CXCR4* expressed on T-cells and macrophages, constituting a functional chemokine-mediated communication axis(Figure 6B-I).

3.7 Spatial-distribution features of FRMD6-AS2-positive cells

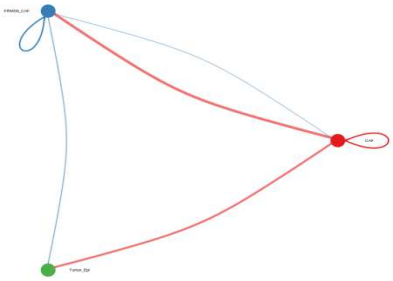
UMAP projection demonstrated evident clustering behaviour among FRMD6-AS2-positive cells, concentrated within a local region of the CAF cluster, suggesting that FRMD6-AS2$^+$ CAFs tend to form focal activated micro-niches, possibly originating from shared-lineage differentiation or local-microenvironment induction. CALM3 expression partially overlapped with FRMD6-AS2$^+$ CAFs; nevertheless, CALM3 was broadly distributed across tumour-epithelial-cell compartments, and their spatial-expression patterns were therefore incompletely concordant.



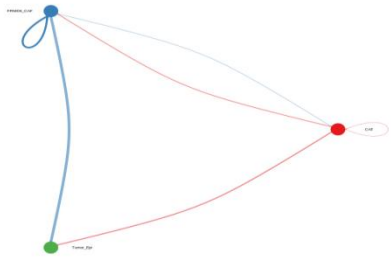
E



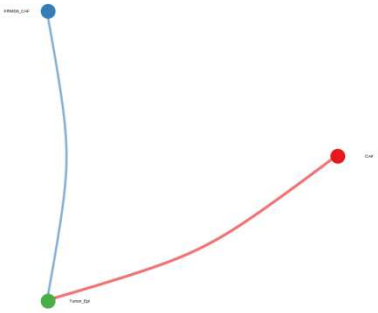
F



G



H



I

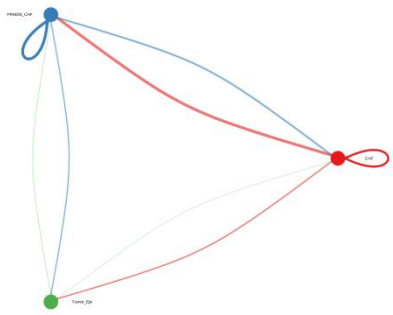


Figure 6 (A) Ridge-plot visualising GSEA-enriched biological-process terms in FRMD6-AS2^{+} CAFs. (B-I) CellChat network diagrams visualising intra-CAF and CAF-to-immune-cell ligand-receptor-mediated communication.

3.8 LASSO-Cox prognostic-model construction, inter-model comparison and external validation

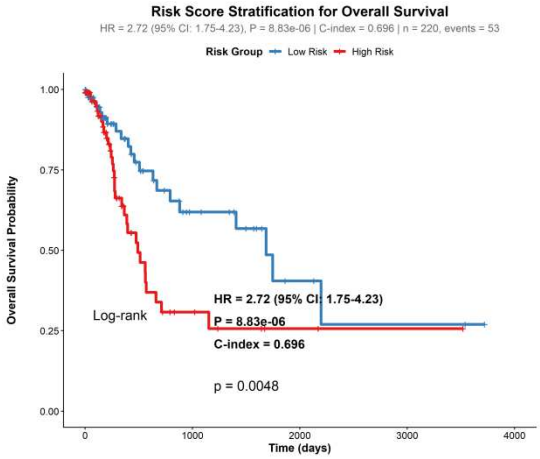
After LASSO-regression variable screening, six predictors (CALM3, FRMD6-AS2, age group, gender, T-stage, N-stage) were retained for risk-score calculation:Risk Score = 0.116 × CALM3 + 0.202 × FRMD6-AS2 + 0.322 × T_stage + 0.377 × N_stage + 0.762 × Age_group + 0.515 × Gender(Figure 7A).

Patients were dichotomised into high-risk and low-risk groups at the median risk-score value. Kaplan-Meier curves demonstrated significantly inferior overall survival for the high-risk subgroup (Log-rank P < 0.001). Treated as a continuous variable, risk-score yielded HR = 3.429 (95 %CI: 2.097-5.606, P < 1e-7), with model C-index = 0.696. Time-dependent ROC analyses yielded 1-year AUC = 0.772, 3-year AUC = 0.732, 5-year AUC = 0.835(Figure 7B-C).

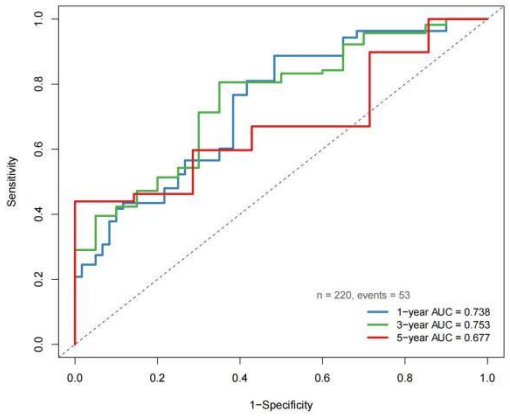
Horizontal inter-model comparisons illustrated that the integrated model combining CALM3-FRMD6-AS2 molecular markers with clinical covariates achieved higher C-index and time-dependent-AUC values relative to the clinical-variable-only base-model. DCA curves demonstrated superior net-clinical-benefit for the integrated model, confirming that CALM3-FRMD6-AS2 expression information delivers incremental prognostic value beyond conventional TNM staging. Multivariate Cox regression identified FRMD6-AS2 (HR = 1.224, P = 0.0375), N-stage and age-group as independent prognostic factors, whereas CALM3 failed to reach statistical significance for independent prognostic prediction (P = 0.538), consistent with its broad epithelial-cell-expression pattern. Notably, LASSO-Cox penalised-regression can retain variables with synergistic predictive utility even if they lack independent prognostic significance, improving overall model performance(Figure 7D-I).

External-cohort validation results: GSE62254 (ACRG): HR = 2.29 (95 %CI: 1.06-4.96, P = 0.036); GSE26253: HR = 1.78 (P = 0.0897); GSE15459: HR = 1.89 (P = 0.0922). Hazard ratios were > 1 across all three external cohorts, showing consistent risk-trends. Differences in sequencing platforms and follow-up-endpoint definitions existed across public cohorts. Sub-group analysis restricted to stage III-IV advanced-disease patients further elevated hazard ratios and reduced P-values, implying that signal-dilution effects originating from rare-CAF-subpopulation features are more pronounced within early-stage gastric-cancer samples and attenuate statistical power(Figure 7J-K).

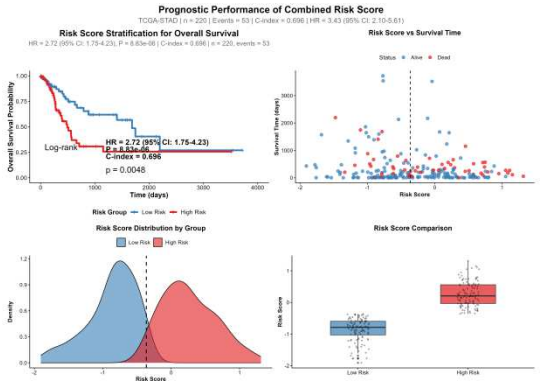
A


Risk Score Stratification for Overall Survival
HR = 2.72 (95% CI: 1.75-4.23), P = 8.83e-06 | C-index = 0.696 | n = 220, events = 53
Risk Group Low Risk High Risk
Overall Survival Probability
Log-rank
HR = 2.72 (95% CI: 1.75-4.23)
P = 8.83e-06
C-index = 0.696
p = 0.0048
Time (days)

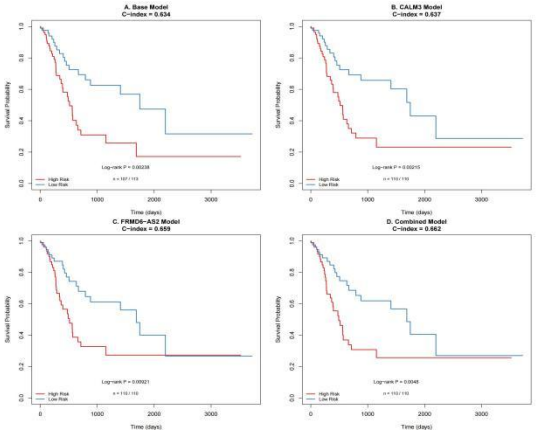
B


Sensitivity
1−Specificity
n = 220, events = 53
1−year AUC = 0.738
3−year AUC = 0.753
5−year AUC = 0.677

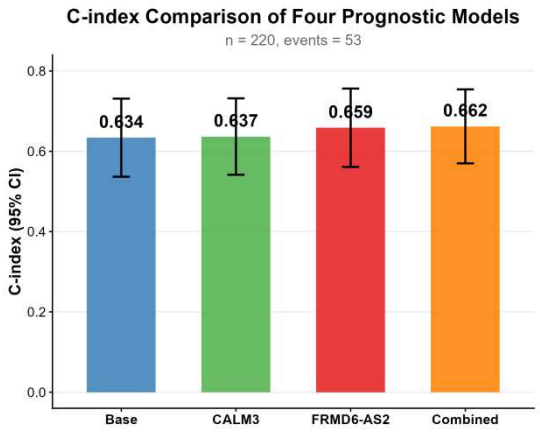
C


Prognostic Performance of Combined Risk Score
Risk Score Stratification for Overall Survival
Risk Score vs Survival Time
Risk Score Distribution by Group
Risk Score Comparison

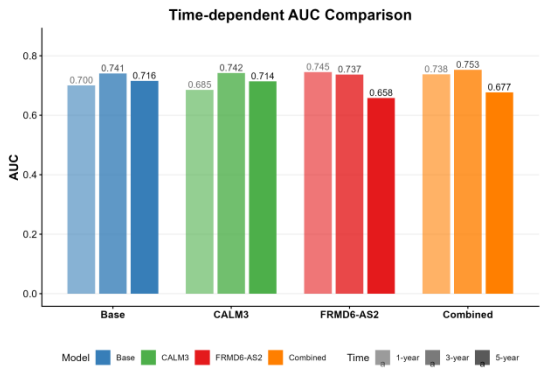
D


A. Base Model
C−index = 0.634
B. CALM3 Model
C−index = 0.637
C. FRMD6−AS2 Model
C−index = 0.659
D. Combined Model
C−index = 0.662

E


C-index Comparison of Four Prognostic Models
n = 220, events = 53
C-index (95% CI)
0.634
0.637
0.659
0.662
Base
CALM3
FRMD6-AS2
Combined

F


Time-dependent AUC Comparison
AUC
0.700
0.741
0.716
0.685
0.742
0.714
0.745
0.737
0.658
0.738
0.753
0.677
Base
CALM3
FRMD6-AS2
Combined
Model
Time
1-year
3-year
5-year

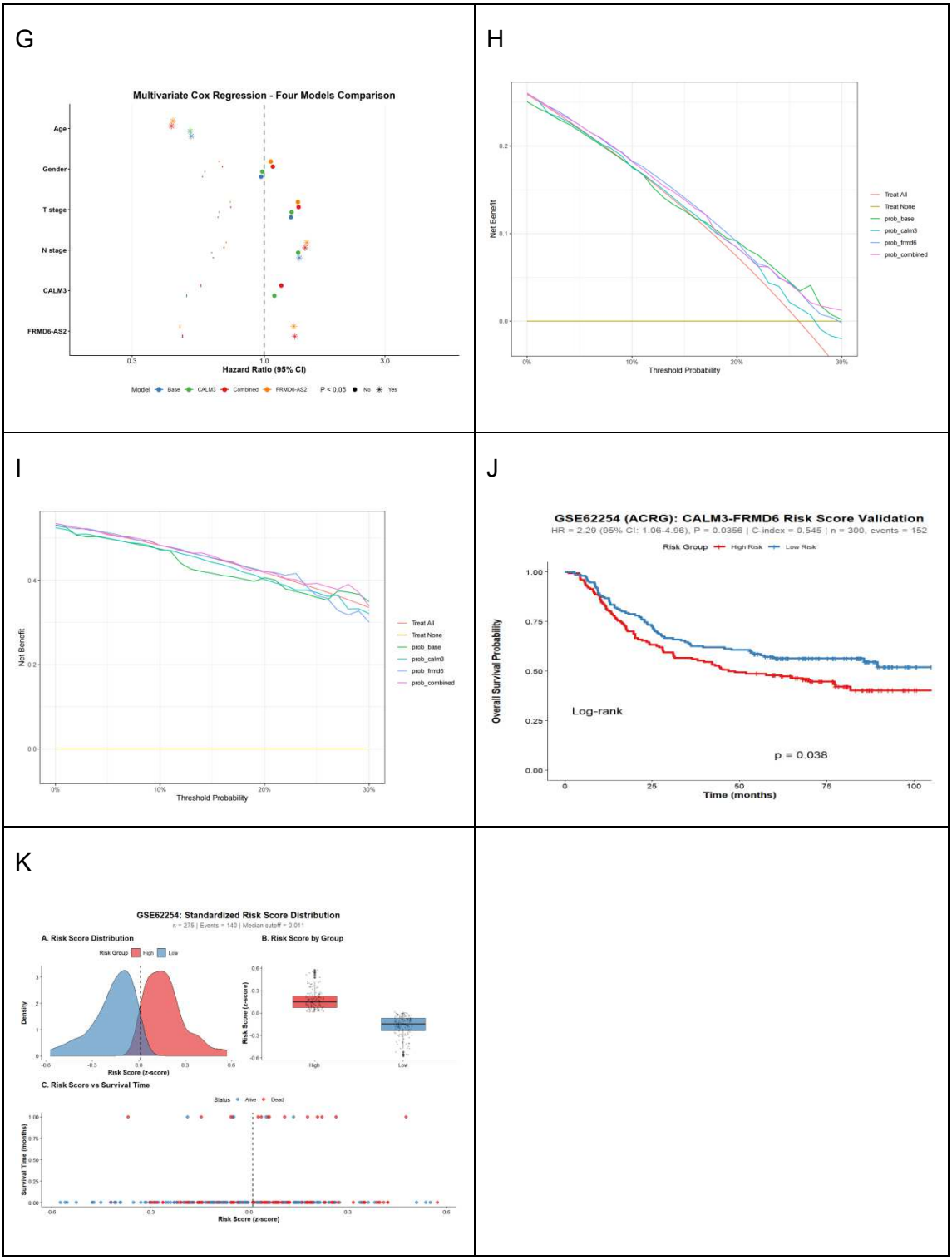
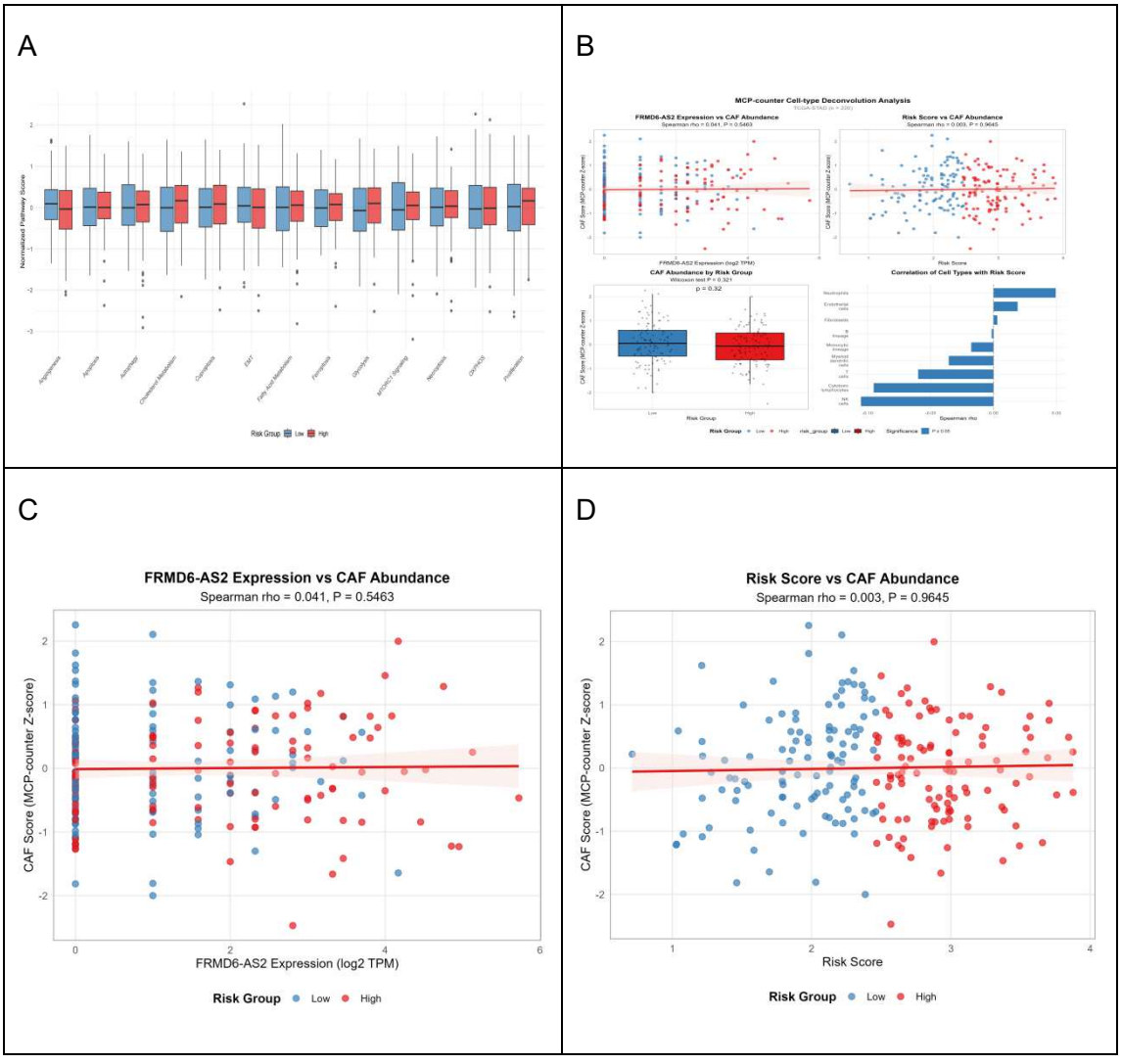


Figure 7 (A) Kaplan-Meier OS survival curve for TCGA-STAD risk-score stratification. (B) Time-dependent ROC curve. (C-D) Composite plots combining KM curves, risk-score distribution, scatter-plots and box-plots. (E) KM-curves for four competing prognostic-models. (F) Bar-chart comparing C-index values across four models. (G) Bar-chart comparing

time-dependent-AUC metrics. (H) Forest-plot for multivariate Cox regression. (I-J) DCA decision-curves at 1-year and 3-year time-horizons. (K-L) KM survival-curves and risk-score-distribution plots for external-validation cohort GSE62254.

3.9 Multi-dimensional bulk-omics association analysis

Summarised results from nine bulk-omics analyses are provided in Supplementary . No statistically-significant inter-group differences (all P > 0.05, FDR > 0.9) were detected between high-risk versus low-risk groups for immune-score, stromal-score, abundance of 67 immune-stromal-cell subsets, expression of 22 immune-checkpoint genes, TMB, or activity of 13 metabolic/cell-death/malignancy-related pathways(Figure 8A). MCP-counter deconvolution showed no significant correlation between FRMD6-AS2 expression / risk-score and global CAF abundance. These data indicate that FRMD6-AS2 marks only an extremely minor functional sub-clade within the broader CAF compartment and cannot reshape global tumour-stromal characteristics(Figure 7B-E).



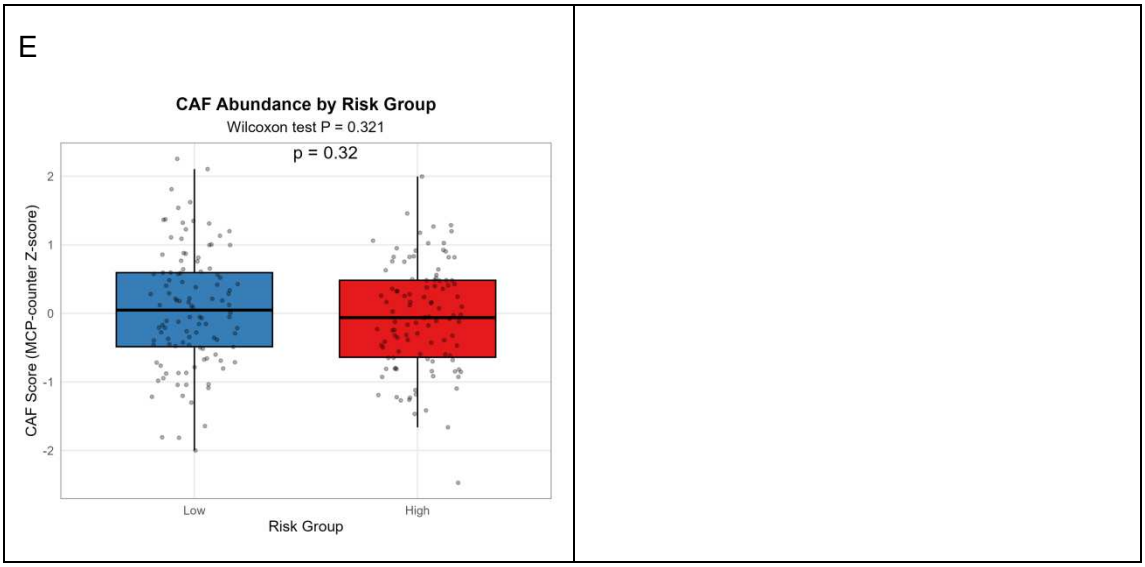
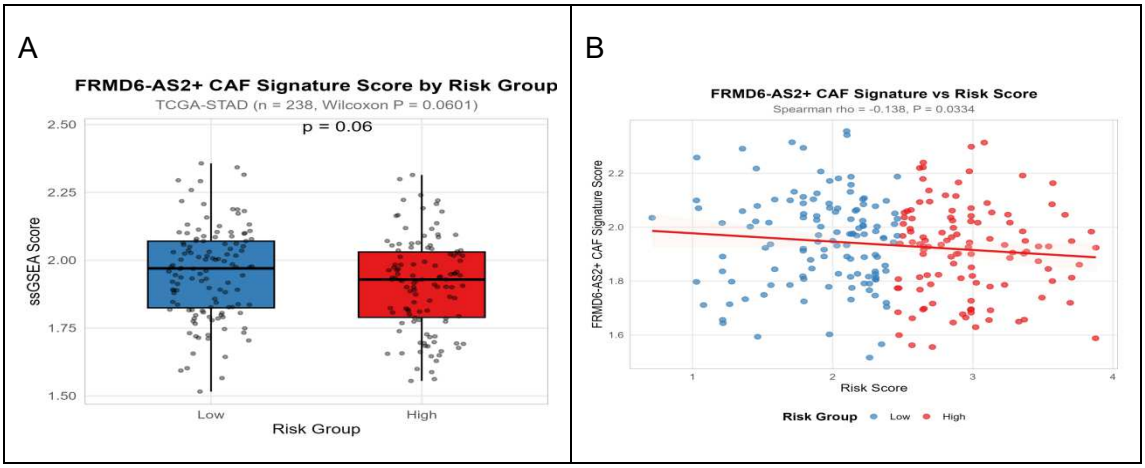


Figure 8 (A) Box-plots comparing pathway-activity scores between high-risk and low-risk subgroups. (B-E) MCP-counter deconvolution outputs: correlation-scatter-plots and box-plots for CAF-abundance versus FRMD6-AS2 expression / risk-score.

3.10 ssGSEA projection of the FRMD6-AS2⁺-CAF-specific signature onto bulk TCGA cohort

Among the 50 signature genes, 44 genes were detected within the TCGA expression matrix (88 % gene-coverage). ssGSEA demonstrated only marginally non-significant differences in signature enrichment scores between high-risk and low-risk groups (Wilcoxon P = 0.0601). The correlation between signature score and risk-score yielded a weak negative Spearman coefficient (*rho* = −0.138, P = 0.0334) with small effect-size; therefore, this correlation cannot be interpreted as biological evidence for tumour-protective effects of FRMD6-AS2⁺ CAFs. These observations further support the rare-subpopulation signal-dilution hypothesis(Figure 9A-C).



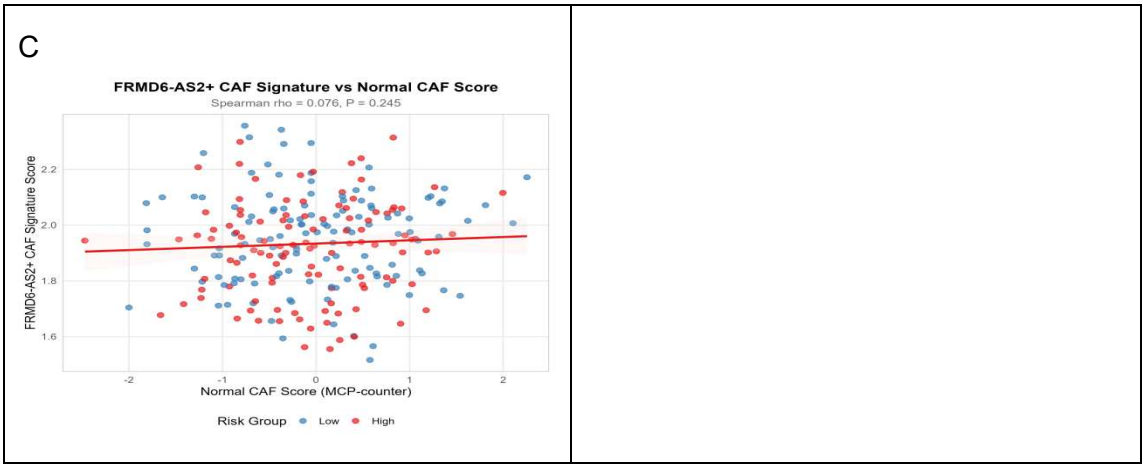


Figure 9 (A) Box-plot comparing FRMD6-AS2⁺-CAF-signature ssGSEA scores across risk subgroups. (B-C) Scatter-plots of signature-score against risk-score and against ordinary MCP-counter-derived CAF-abundance scores.

3.11 Single-cell in silico perturbation and rescue simulations dissecting the CALM3-FRMD6-AS2 regulatory mechanism

3.11.1 Linear-correlation characteristics between FRMD6-AS2 and CALM3

Based on expression data exclusively from the 52 FRMD6-AS2-positive cells, mean FRMD6-AS2 expression = 1.0571 and mean CALM3 expression = 1.9286. Fitted linear-regression equation:$CALM3 = 0.6061 \times FRMD6 - AS2 + 1.2879$, , coefficient of determinationR^2=0.0068. Despite extremely poor simple-linear-model fit, gradient in-silico-knockdown simulations observed mild dose-dependent down-regulation of CALM3 upon FRMD6-AS2 reduction, suggesting indirect, non-linear regulatory effects exerted by FRMD6-AS2 on CALM3 rather than canonical linear upstream-downstream transcriptional relationships.

Gradient in-silico-knockdown results demonstrated progressive dose-dependent reduction of CALM3 as FRMD6-AS2 expression was repressed: 30 % knockdown: −5.02 % CALM3 change; 50 % knockdown: −8.36 %; 70 % knockdown: −11.70 %; 90 % severe knockdown: −15.05 %; 99 % maximal-extent knockdown: maximal CALM3 reduction reached −16.55 %. These results support positive regulatory influence of FRMD6-AS2 upon CALM3, mediated via indirect non-linear modes, consistent with the low R^2 value from linear fitting(Figure 10A).

.

3.11.2 FRMD6-AS2 knockdown triggers malignant EMT reprogramming

A 90 % in-silico FRMD6-AS2 knockout induced comprehensive EMT-program activation and collapse of epithelial identity. Key molecular alterations included: ① Collapse of the core epithelial axis: ZEB1 decreased by 62.60 %, CDH1 plummeted by 93.41 %, leading to complete loss of epithelial integrity; ② Robust activation of mesenchymal programmes: CDH2 (+100.91 %), FN1 (+66.95 %), VIM (+37.90 %) were markedly up-regulated; ③ Moderate activation of EMT-transcription factors SNAI1 and TWIST1. Collectively, these changes represented typical malignant mesenchymal-transition signatures. Top-ranked perturbed genome-wide genes included EMT-effector genes such as FN1, further validating that FRMD6-AS2 loss potently drives mesenchymal malignant progression(Figure 10B).

.

3.11.3 Gradient CALM3 rescue cannot reverse FRMD6-AS2-depletion-mediated EMT damage

Under the background of 90 % FRMD6-AS2 knockout, 2-fold, 5-fold and 10-fold virtual CALM3 over-expression efficiently restored CALM3 transcript abundance. CALM3 rescue could partially ameliorate mesenchymal-associated gene phenotypes yet failed to rescue epithelial-compartment injury: ZEB1 and CDH1 expression showed no restorative trend; CDH1-mediated epithelial damage was even further aggravated. Only very modest improvements were observed for mesenchymal-effector genes *VIM*, *FN1* and *CDH2*(Figure 10C-D).

These simulation outcomes suggest non-complementary,non-simple-upstream-downstream functional relationships between CALM3 and FRMD6-AS2. FRMD6-AS2 predominantly governs the ZEB1-CDH1 epithelial-plasticity axis, while CALM3 specifically modulates the *VIM*/*FN1* mesenchymal-migration axis; they operate via a parallel-synergistic dual-pathway regulatory mode.

3.11.4 EMT-gene correlation analysis corroborates the dual-axis regulatory-model

Within FRMD6-AS2-positive cells, Pearson correlation analysis revealed moderate statistically-significant positive correlations between CALM3 and mesenchymal markers: *VIM* ($r = 0.4391$, $P < 0.001$), *CDH2* ($r = 0.3390$, $P = 0.004$), *FN1* ($r = 0.3238$, $P = 0.006$). In contrast, CALM3 exhibited no significant correlation with epithelial-transcription factors ZEB1 and SNAI1 ($P > 0.05$). These findings are consistent with the dual-axis regulatory model: CALM3 is predominantly correlated with mesenchymal-effector genes, whereas FRMD6-AS2 is mainly associated with epithelial-regulatory genes, suggesting that they may cooperatively participate in EMT regulation through distinct pathways.(Figure 10E-F).

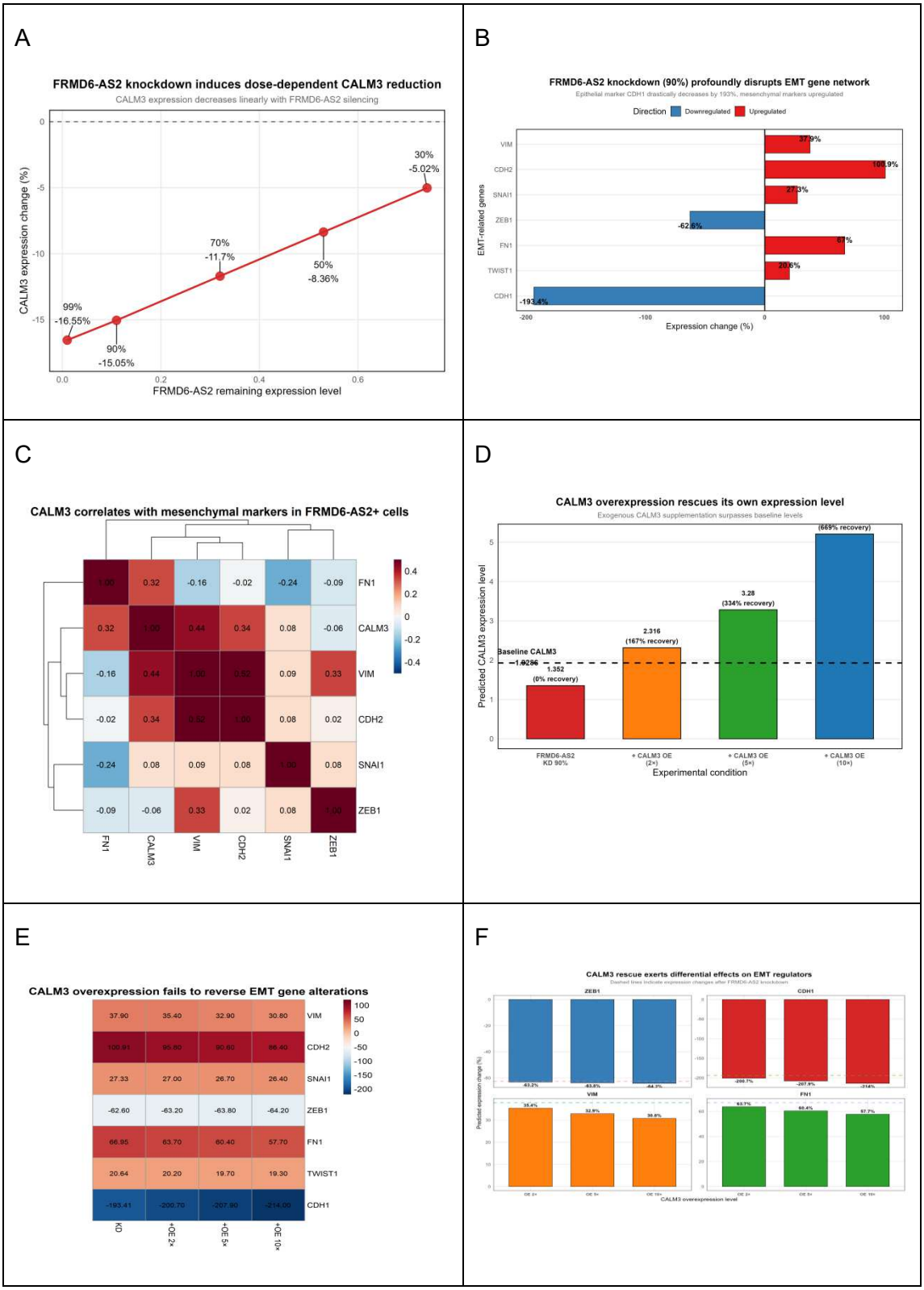


Figure 10 (A) Dose-response curve showing CALM3 expression-change versus remaining FRMD6-AS2 expression upon in-silico knockdown. (B) Bar-chart illustrating EMT-gene-expression changes after 90 % FRMD6-AS2

knockout. (C) Correlation heat-map among CALM3 and EMT-related genes in FRMD6-AS2^{+} cells. (D) Bar-chart for CALM3-expression-recovery efficiency upon gradient CALM3 rescue under FRMD6-AS2-knockout background. (E) Heat-map summarising EMT-gene responses to increasing CALM3 rescue dosage. (F) Composite bar-plots showing differential rescue effects on ZEB1, CDH1, VIM and FN1.

3.12 Wet-laboratory functional assays validate biological effects of FRMD6-AS2 knockdown and CALM3 over-expression

qPCR verified transfection efficiency and downstream CALM3 expression changes. qPCR assays confirmed that relative FRMD6-AS2 expression in the si-LincRNA group decreased to 0.34-fold relative to the siNC group ($P < 0.001$), confirming efficient knockdown. In the oeCALM3 group, CALM3 relative expression increased to 1.92-fold compared with the oeNC group ($P < 0.001$), verifying successful over-expression. qPCR further demonstrated that CALM3 over-expression up-regulated FRMD6-AS2 expression by 2.59-fold, pointing towards positive regulatory crosstalk from CALM3 towards FRMD6-AS2, although their functions are partially independent and cannot fully compensate for one-another. Amplification and melting-curves validated qPCR-data reliability(Figure 11A-B).

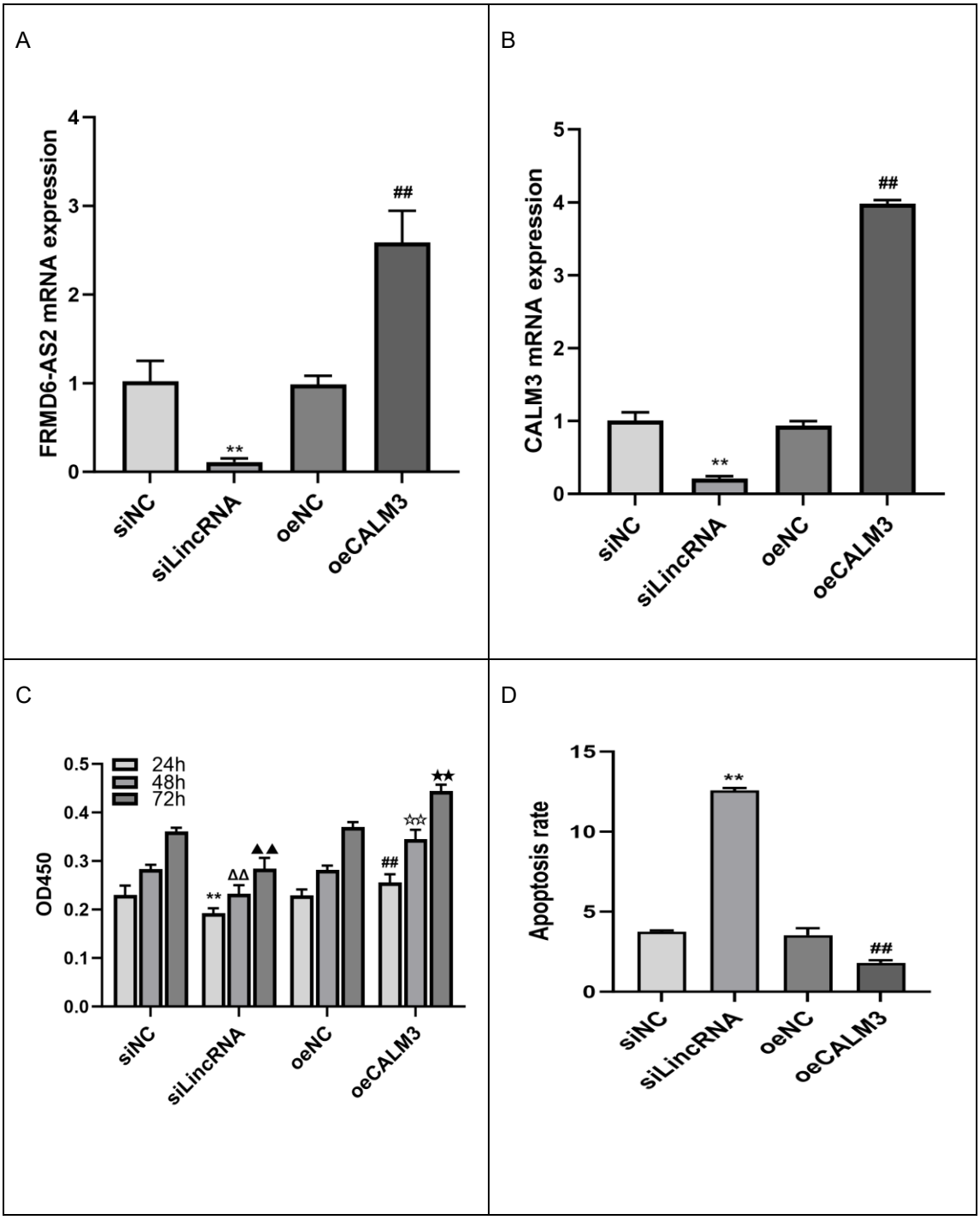
CCK-8 proliferation assays: Compared against the siNC group, HGC-27 proliferative capacity was significantly weakened in the si-LincRNA group: OD_{450} value dropped to 0.308 at the 72-h time-point ($P < 0.01$), indicating that FRMD6-AS2 loss inhibits gastric-cancer-cell proliferation. Conversely, oeCALM3-group proliferation was significantly enhanced; OD_{450} reached 0.466 at 72 h versus oeNC-group 0.383 ($P < 0.01$). These results demonstrate that FRMD6-AS2 knockdown suppresses HGC-27 proliferation whereas CALM3 over-expression promotes proliferation(Figure 11C).

Flow-cytometry apoptosis-detection assays: Total apoptotic rate (early + late apoptosis) in the si-LincRNA group reached 12.57 ± 0.17 %, significantly higher than 3.75 ± 0.09 % for siNC ($P < 0.01$). The oeCALM3-group apoptotic rate decreased to 1.80 ± 0.17 %, compared with oeNC-group 3.53 ± 0.44 % ($P < 0.001$). This shows that FRMD6-AS2 depletion promotes HGC-27 apoptosis and CALM3 over-expression represses apoptosis(Figure 11D).

Scratch-wound-healing migration assays: The 24-h wound-healing ratio for si-LincRNA-transfected HGC-27 cells was 28.46 ± 2.87 %, significantly higher than siNC-group 10.29 ± 1.54 % ($P < 0.001$). The oeCALM3 group achieved a 27.56 ± 2.63 % healing ratio, significantly elevated compared with oeNC ($P < 0.001$). Thus, FRMD6-AS2 knockdown enhances migratory potential and CALM3 over-expression augments cell migration(Figure 11E).

Integrated interpretation of wet-laboratory, in-silico-perturbation results: Collectively, qPCR, CCK-8, flow-cytometry and scratch-wound-healing data show that FRMD6-AS2 knockdown inhibits HGC-27 proliferation, promotes apoptosis and enhances migratory capacity. CALM3 over-expression exerts opposite phenotypes: it promotes proliferation, represses apoptosis

and strengthens migration. CALM3 over-expression can only partially rescue phenotypes induced by FRMD6-AS2 loss and cannot achieve complete reversal. Wet-laboratory findings support the “parallel-synergistic, non-replaceable” CALM3-FRMD6-AS2 regulatory-model derived from single-cell in-silico knockout-and-rescue simulations.



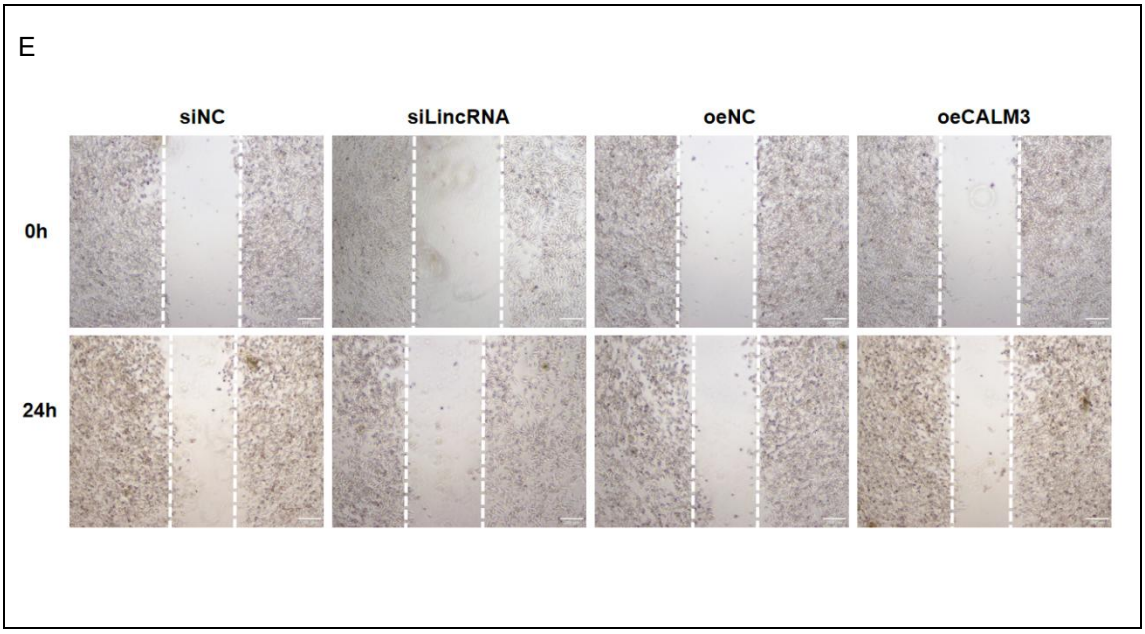


Figure 11 (A-B) qPCR relative-expression bar-plots for FRMD6-AS2 and CALM3 across four experimental groups. (C) CCK-8 proliferation-assay OD-value bar-plot (24 h, 48 h, 72 h). (D) Bar-plot summarising flow-cytometry-derived total-apoptosis rates. (E) Representative scratch-wound-healing micrographs at 0 h and 24 h post-scratch for each experimental condition.

4 Discussion

Gastric-cancer manifests profound tumour-microenvironment heterogeneity. Cancer-associated fibroblasts (CAFs) constitute the functionally most complex stromal-cell population within the TME. Accumulating evidence confirms extensive functional heterogeneity inside the CAF compartment; a small subset of rare malignant CAF subpopulations act as key drivers of tumour invasion, metastasis and immune-microenvironment remodelling[22]. Nevertheless, core molecular axes governing activation and functional reprogramming of these rare malignant CAF subsets remain incompletely characterised.

In the present study, we integrated TCGA bulk-transcriptome data and the GSE183904 single-cell-transcriptome dataset. Candidate CALM3-FRMD6-AS2 interactions were screened by combining WGCNA co-expression-network analysis and multiple RBP-lncRNA-binding-prediction algorithms. We deciphered transcriptional and microenvironmental features specific for the FRMD6-AS2^{+} rare malignant-CAF subset. Single-cell gradient in-silico-knockout and CALM3 rescue simulations uncovered for the first time their parallel-synergistic mechanism controlling EMT regulation. A robust prognostic risk-model was built and externally validated across multiple independent public cohorts. We systematically interpreted the signal-dilution mechanism reconciling EMT-pathway-activation

observed at single-cell resolution with negative bulk-omics outputs. Our study delivers new theoretical insights into gastric-cancer CAF heterogeneity and provides candidate molecular targets for stroma-directed therapeutic development.

CALM3 is a classic calmodulin-family protein canonically responsible for calcium-signal transduction. Recent publications uncovered its non-canonical RNA-binding-protein activity: it can bind lncRNAs to modulate post-transcriptional transcript regulation and participates in gastrointestinal-tumour progression[23]. However, prior work had not defined its lncRNA binding partners nor its functional roles within the gastric-cancer TME, particularly within CAF subpopulations. FRMD6-AS2 represents an antisense lncRNA transcribed from the *FRMD6* locus; previous studies implicated it in Hippo-pathway modulation, yet its cell-specific expression patterns, biological functions and molecular-regulatory roles within gastric-cancer and CAF subsets were unreported. In our work, three independent bioinformatic algorithms (catRAPID, RPISeq, RBPSuite-2.0) collectively predicted high-confidence potential physical interaction between CALM3 protein and FRMD6-AS2 RNA, supplying molecular-computational evidence supporting formation of putative RBP-lncRNA complexes.

Single-cell transcriptomic profiling revealed broad CALM3 expression across tumour-epithelial-cell populations together with partial expression within subsets of stromal CAFs. In sharp contrast, FRMD6-AS2 exhibited strict cell-subpopulation-specific expression and was detected in merely 0.034 % of total cells, the overwhelming majority of FRMD6-AS2-positive cells localising to CAF clusters and only a tiny fraction localising to T-cells. Their spatial-expression patterns were only partially overlapping. RBP proteins are frequently broadly expressed multifunctional molecules, while their target lncRNAs often display stringent cell-subset-specific restriction[24]. Molecular physical interaction represents an intracellular event, requiring only co-occurrence of both molecules inside the identical cell to take place. Within FRMD6-AS2^{+} CAFs, approximately 75 % of FRMD6-AS2-positive cells co-expressed CALM3, furnishing a cellular context permissive for molecular interaction. In tumour-epithelial-cell compartments, CALM3 is abundantly expressed yet FRMD6-AS2 is nearly absent; under these circumstances CALM3 executes its canonical calcium-signalling functions and does not engage in FRMD6-AS2-related post-transcriptional regulatory programmes. FRMD6-AS2^{+} CAFs harboured ALDH-associated stem-like metabolic signatures; CellChat analyses predicted strong intra-subset self-communication as well as bidirectional immune-crosstalk between FRMD6-AS2^{+} CAFs and T-cells / macrophages, indicating that this rare CAF subset not only mediates stromal-matrix remodelling but also participates in reshaping tumour-immune-cell-interaction landscapes.

To dissect CALM3-FRMD6-AS2 regulatory logic, we performed single-cell gradient in-silico-knockdown and CALM3-rescue perturbation analyses using exclusively FRMD6-AS2-positive CAF-cell profiles. Linear-regression fitting yielded$R^2=0.0068$, demonstrating negligible simple-linear-transcriptional correlation between CALM3 and FRMD6-AS2. Nevertheless, gradient-knockdown simulations observed mild dose-dependent CALM3 down-regulation upon progressive FRMD6-AS2 repression, pointing towards indirect non-linear regulatory effects rather than canonical unidirectional upstream-downstream transcriptional cascades. A 90 % virtual FRMD6-AS2 knockout triggered collapse of the

ZEB1-CDH1 epithelial axis and comprehensive activation of mesenchymal-marker genes, driving malignant EMT-reprogramming. Critically, CALM3 gradient rescue under FRMD6-AS2-knockout background could not restore ZEB1-CDH1-mediated epithelial-cell identity and exerted only modest amelioration of selected mesenchymal-gene phenotypes. These perturbation-simulation-derived findings strongly support non-mutually-compensatory functions for CALM3 versus FRMD6-AS2: FRMD6-AS2 primarily sustains the ZEB1-CDH1 epithelial-plasticity axis, whereas CALM3 preferentially governs *VIM*/*FN1*/*CDH2* mesenchymal-migration-related genes, and they cooperatively drive CAF-associated EMT-progression via a parallel-synergistic regulatory-mode.

Notably, our single-cell in-silico-perturbation analyses were computed within FRMD6-AS2^{+} CAF-cell transcriptomes; maximal CALM3 reduction upon complete FRMD6-AS2 in-silico-knockout only reached 16.55 %. By contrast, si-mediated FRMD6-AS2 knockdown in HGC-27 gastric-tumour-epithelial-cells produced substantially larger-magnitude CALM3 mRNA down-regulation. This discrepancy highlights divergent molecular-response amplitudes under distinct cellular-context backgrounds. Our wet-laboratory functional validations were performed in the HGC-27 gastric-cancer-epithelial-tumour-cell line, which possesses extremely low endogenous FRMD6-AS2 transcript abundance and is not a native CAF cell-type. Phenotypes observed in HGC-27 therefore reflect biological responses elicited by this molecular axis within gastric-tumour-epithelial-cells but cannot perfectly recapitulate authentic molecular-interaction events occurring inside CAFs. Although phenotypic directions from wet-cell-culture assays are broadly concordant with single-cell-simulation outputs, future studies employing primary human gastric-cancer-derived CAFs, RIP-seq assays and RNAscope in-situ hybridisation-immunofluorescence co-localisation are required to directly validate physical CALM3-FRMD6-AS2 interaction and downstream functional consequences within authentic CAF-cells.

The LASSO-Cox-based prognostic risk-score combined CALM3, FRMD6-AS2 and clinical-pathological covariates exhibited favourable survival-predictive performance in the TCGA-STAD discovery cohort and maintained consistent risk-trends across multiple GEO external-validation cohorts. In multivariate Cox regression, CALM3 did not attain statistical-significance as an independent prognostic-predictor; nevertheless, LASSO-Cox penalised-regression retained CALM3 within the final risk-formula. This observation is compatible with LASSO-algorithm properties: LASSO can retain variables conferring synergistic predictive gain even when individual variables lack independent-prognostic-significance, and inclusion of CALM3 improved overall model predictive power. Because CALM3 is broadly expressed across tumour-epithelial-cells and FRMD6-AS2 is restricted to a rare CAF subset, risk-scores derived from bulk-transcriptome data integrate transcriptional signals originating both from tumour-epithelial-cells and from rare FRMD6-AS2^{+} CAFs. Consequently, prognostic performance of the risk-model cannot be fully attributed exclusively to the FRMD6-AS2^{+} CAF sub-population. ssGSEA scores for our FRMD6-AS2^{+}-CAF-specific signature achieved only borderline statistical-difference ($P = 0.0601$) between risk-score-stratified subgroups in bulk TCGA data. This observation is consistent with our rare-subpopulation signal-dilution hypothesis, yet further validation using larger spatial-transcriptomic patient-cohorts remains warranted.

Aberrant EMT-program-activation represents a core molecular-event driving gastric-cancer invasion and metastasis. A large-body-of-literature describes EMT-induction of tumour-epithelial-cells by CAF-secreted paracrine-factors[25]. Additionally, CAFs themselves can undergo EMT-like reprogramming to promote stromal-matrix remodelling. Our work suggests that inside FRMD6-AS2^{+} malignant-CAF subsets, the CALM3-FRMD6-AS2 parallel-synergistic axis can concurrently regulate epithelial-plasticity and mesenchymal-migration-gene-modules to facilitate CAF malignant-reprogramming. Our study expands mechanistic understanding regarding RBP-lncRNA regulatory-modes operating within tumour-stromal-compartments: RBPs are not necessarily fixed upstream components of linear signalling cascades, and lncRNAs are not merely passive downstream-effect-molecules[26]. Instead, they can functionally partition control over distinct EMT sub-programmes and cooperate to boost oncogenic malignant progression.

Several important limitations of this study should be acknowledged. First, evidence supporting physical CALM3-FRMD6-AS2 interaction originates exclusively from multiple bioinformatic-prediction pipelines; direct biochemical experimental evidence such as RIP-seq or RNA-pull-down assays is absent. Second, in-vitro functional validation experiments were performed using the tumour-epithelial-cell-line HGC-27; functional assays in primary patient-derived gastric-cancer CAFs as well as in-vivo animal-model experiments are still needed to verify in-tumour-growth and metastatic phenotypes driven by this molecular axis. Third, prognostic-model construction and validation are entirely based on publicly-available transcriptomic-dataset resources; prospective independent clinical-patient-cohorts originating from our own institution are lacking for prospective-validation purposes. Fourth, single-cell in-silico gene-perturbation represents a computational-simulation approach and cannot fully replace genuine gene-knockout / over-expression wet-laboratory experiments.

From a translational-research perspective, FRMD6-AS2^{+} CAFs constitute an extremely rare pro-oncogenic stromal-subpopulation that cannot be readily captured by conventional bulk-sequencing assays. Future spatial-transcriptomics and single-cell-sequencing technologies will assist in deciphering dynamic changes of this stromal-subset across different gastric-cancer disease-stages. The CALM3-FRMD6-AS2-derived prognostic risk-score supplies supplementary references for survival-stratification of gastric-cancer patients; nevertheless, real-world-patient-cohort validations are still required prior to clinical-implementation.

In summary, via multi-omics-integrated analyses, we identified a novel RBP-lncRNA parallel-synergistic regulatory-axis CALM3-FRMD6-AS2 in gastric-cancer, which marks the functionally important rare malignant FRMD6-AS2^{+} CAF sub-population. FRMD6-AS2 governs epithelial-plasticity through the ZEB1-CDH1 axis, and CALM3 modulates mesenchymal-migration-related pathways; together they cooperate to facilitate EMT-associated malignant progression of gastric cancer. Our study provides new mechanistic insights into gastric-cancer CAF heterogeneity and delivers theoretical clues for developing stroma-targeted anti-tumour therapeutic candidates.

Acknowledgements

Not applicable.

Funding

No funding

Availability of data and materials

The datasets analysed in this study are publicly available. The Cancer Genome Atlas stomach adenocarcinoma (TCGA-STAD) data were obtained from the Genomic Data Commons (GDC) Data Portal at https://portal.gdc.cancer.gov/projects/TCGA-STAD (project TCGA-STAD). The single-cell RNA-sequencing and bulk transcriptomic datasets were retrieved from the Gene Expression Omnibus (GEO) under the following accession numbers, each with a direct link to the corresponding dataset:
GSE183904 (https://www.ncbi.nlm.nih.gov/geo/query/acc.cgi?acc=GSE183904),
GSE62254 (https://www.ncbi.nlm.nih.gov/geo/query/acc.cgi?acc=GSE62254),
GSE26253 (https://www.ncbi.nlm.nih.gov/geo/query/acc.cgi?acc=GSE26253),
GSE15459 (https://www.ncbi.nlm.nih.gov/geo/query/acc.cgi?acc=GSE15459). All other publicly available datasets used in this study are cited and described in the Materials and Methods section. The R and Python analysis scripts used in this study are available from the first author (Fan Luo, luof2024@lzu.edu.cn) upon reasonable request.

Supplementary materials

Supplementary tables, supplementary figures, original qPCR Ct raw data and additional output from single-cell in-silico perturbation analyses are provided as supplementary materials accompanying this article.

Authors' contributions

FL and MR conceived and designed the research study. FL and LYC performed bioinformatic analyses and drafted the original manuscript. XLS and JL prepared all figures and tables. YLW and MR critically revised the manuscript for important intellectual content. MR supervised the whole project and verified the authenticity of all raw experimental and bioinformatic data. All authors have read and approved the final submitted manuscript.

Declarations

Ethics approval and Accordance:

Not applicable. This study did not involve human participants, human tissues, or animals; the work was conducted entirely using publicly available, de-identified database datasets (TCGA-STAD and GEO) and established in vitro cell line models, and therefore no ethics committee approval was required.

Consent to participate:

Not applicable.

Consent to publish:

Not applicable.

Competing interests

The authors declare that they have no competing interests.

Use of artificial-intelligence-assisted tools

During manuscript preparation, the authors utilised the Yujing AI-assisted Research System (Yujing Medicine Technology, Shenzhen, China) for literature retrieval, English-grammar checking and textual polishing. All AI-processed text was manually reviewed, revised and edited by human authors, who take full responsibility for the complete content of this manuscript. No artificial-intelligence tools were employed for raw-data analysis, plotting of scientific figures, statistical computation or generation of scientific conclusions. No AI system qualifies for authorship and is not listed among the authors.

References

[1] Bray F, Laversanne M, Sung H, et al. Global cancer statistics 2022: GLOBOCAN estimates of incidence and mortality worldwide for 36 cancers in 185 countries. CA Cancer J Clin. 2024;74:229–263.

[2] Bilotta MT, Antignani A, Fitzgerald DJ. Managing the TME to improve the efficacy of cancer therapy. Front Immunol. 2022 Oct 20;13:954992.

[3] Bejarano L, Jordão MJC, Joyce JA. Therapeutic Targeting of the Tumor Microenvironment. Cancer Discov. 2021 Apr;11(4):933-959.

[4] Peng C, Xu Y, Wu J, et al. TME-Related Biomimetic Strategies Against Cancer. Int J Nanomedicine. 2024 Jan 4;19:109-135.

[5] Sahai E, Astsaturov I, Cukierman E, et al. A framework for advancing our understanding of cancer-associated fibroblasts. Nat Rev Cancer, 2020,20(3):174-186.

[6] Yu L, Shen N, Shi Y, et al. Characterization of cancer-related fibroblasts (CAF) in hepatocellular carcinoma and construction of CAF-based risk signature based on single-cell RNA-seq and bulk RNA-seq data. Front Immunol. 2022 Sep 23;13:1009789.

[7] Zhang X, Ren B, Liu B, et al. Single-cell RNA sequencing and spatial transcriptomics reveal the heterogeneity and intercellular communication of cancer-associated fibroblasts in gastric

cancer. J Transl Med. 2025 Mar 18;23(1):344.

[8] Li MQ, Wang SK, Xiao H,et al. The FAP+ CAF subset in bladder cancer: A key driver of cancer cell stemness and a promising target for FAPI therapy. Clin Transl Discov. 2026;6(4):e70179.

[9] Chen GX, Yu CX, Tang ZC, et al. Metformin suppresses gastric cancer progression through calmodulin-like protein 3 secreted from tumor-associated fibroblasts. Oncol Rep. 2019;41(1):405-414.

[10] Liao JY, Yang B, Shi CP, et al. RBPWorld for exploring functions and disease associations of RNA-binding proteins across species. Nucleic Acids Res. 2025 Jan 6;53(D1):D220-D232.

[11] Wang J, Li Z, Wang X, et al. The tumor suppressive effect of long non-coding RNA FRMD6-AS2 in uteri corpus endometrial carcinoma. Life Sci. 2020 Feb 15;243:117254.

[12] Tan X, Mao L, Huang C, et al. Comprehensive analysis of lncRNA-miRNA-mRNA regulatory networks for microbiota-mediated colorectal cancer associated with immune cell infiltration. Bioengineered. 2021 Dec;12(1):3410-3425.

[13] Pastushenko I, Blanpain C. EMT Transition States during Tumor Progression and Metastasis. Trends Cell Biol. 2019 Mar;29(3):212-226.

[14] Biskupski M, Brachet A, Hunek G, et al. Gastric Cancer Epithelial-Mesenchymal Transition-The Role of Micro-RNA. Cancers (Basel). 2026 Jan 30;18(3):462.

[15] Mittal V. Epithelial Mesenchymal Transition in Tumor Metastasis. Annu Rev Pathol. 2018 Jan 24;13:395-412.

[16] Otake S, Itoh Y, Saitoh M, et al. TGF-β downregulates E-cadherin expression via a novel ZEB1-dependent mechanism. J Biochem. 2026 Oct 1;180(4):319-328.

[17] Dong D, Na L, Zhou K, et al. FZD5 prevents epithelial-mesenchymal transition in gastric cancer. Cell Commun Signal. 2021 Feb 22;19(1):21.

[18] Colaprico A, Silva TC, Olsen C,et al. TCGAbiolinks: an R/Bioconductor package for integrative analysis of TCGA data. Nucleic Acids Res. 2016 May 5;44(8):e71.

[19] Navarro Gonzalez J, Zweig AS, Speir ML, et al. The UCSC Genome Browser database: 2021 update. Nucleic Acids Res. 2021 Jan 8;49(D1):D1046-D1057.

[20] Langfelder P, Horvath S. WGCNA: an R package for weighted correlation network analysis. BMC Bioinformatics. 2008 Dec 29;9:559.

[21] Kumar V, Ramnarayanan K, Sundar R, et al. Single-Cell Atlas of Lineage States, Tumor

Microenvironment, and Subtype-Specific Expression Programs in Gastric Cancer. Cancer Discov. 2022;12(3):670-691.

[22] Guo T, Xu J. Cancer-associated fibroblasts: a versatile mediator in tumor progression, metastasis, and targeted therapy. Cancer Metastasis Rev. 2024 Sep;43(3):1095-1116.

[23] Hentze MW, Castello A, Schwarzl T, et al. A brave new world of RNA-binding proteins. Nat Rev Mol Cell Biol. 2018 May;19(5):327-341.

[24] Statello L, Guo CJ, Chen LL,et al. Gene regulation by long non-coding RNAs and its biological functions. Nat Rev Mol Cell Biol. 2021 Feb;22(2):96-118.

[25] Yu Y, Xiao CH, Tan LD, et al. Cancer-associated fibroblasts induce epithelial-mesenchymal transition of breast cancer cells through paracrine TGF-β signalling. Br J Cancer. 2014 Feb 4;110(3):724-32.

[26] Li L, Miao H, Chang Y,et al. Multidimensional crosstalk between RNA-binding proteins and noncoding RNAs in cancer biology. Semin Cancer Biol. 2021 Oct;75:84-96.